ViDA: a Vlasov-DArwin solver for plasma physics at electron scales

Oreste Pezzi, Giulia Cozzani, Francesco Califano, Francesco Valentini, Massimiliano Guarrasi, Enrico Camporeale, Gianfranco Brunetti, Alessandro Retinò, Pierluigi Veltri

ViDA: a Vlasov-DArwin solver for plasma physics at electron scales

Oreste Pezzi[1,2,3]†, Giulia Cozzani[4,5], Francesco Califano[4], Francesco Valentini[3], Massimiliano Guarrasi[6], Enrico Camporeale[7,8], Gianfranco Brunetti[3], Alessandro Retinò[5] and Pierluigi Veltri[3]

[1]Gran Sasso Science Institute, Viale F. Crispi 7, I-67100 LAquila, Italy

[2]INFN/Laboratori Nazionali del Gran Sasso, Via G. Acitelli 22, I-67100 Assergi (AQ), Italy

[3]Dipartimento di Fisica, Università della Calabria, Via P. Bucci, I-87036 Arcavacata di Rende (CS), Italy

[4]Dipartimento di Fisica "E. Fermi", Università di Pisa, Largo B. Pontecorvo 3, I-56127 Pisa, Italy

[5]Laboratoire de Physique des Plasmas, CNRS/École Polytechnique/Sorbonne Université, Université Paris Sud, Observatoire de Paris, 91128 Palaiseau, France

[6]CINECA Interuniversity Consortium, Via Magnanelli 6/3, 40033 Casalecchio di Reno, Italy

[7]CIRES, University of Colorado, Boulder, CO, USA

[8]Center for Mathematics and Computer Science (CWI), 1090 GB Amsterdam, The Netherlands

(Received xx; revised xx; accepted xx)

We present a Vlasov-DArwin numerical code (ViDA) specifically designed to address plasma physics problems, where small-scale high accuracy is requested even during the non linear regime to guarantee a clean description of the plasma dynamics at fine spatial scales. The algorithm provides a low-noise description of proton and electron kinetic dynamics, by splitting in time the multi-advection Vlasov equation in phase space. Maxwell equations for the electric and magnetic fields are reorganized according to Darwin approximation to remove light waves. Several numerical tests show that ViDA successfully reproduces the propagation of linear and nonlinear waves and captures the physics of magnetic reconnection. We also discuss preliminary tests of the parallelization algorithm efficiency, performed at CINECA on the Marconi-KNL cluster. ViDA will allow to run Eulerian simulations of a non-relativistic fully-kinetic collisionless plasma and it is expected to provide relevant insights on important problems of plasma astrophysics such as, for instance, the development of the turbulent cascade at electron scales and the structure and dynamics of electron-scale magnetic reconnection, such as the electron diffusion region.

1. Introduction

Despite being studied with great efforts for about a century, natural and laboratory plasmas exhibit several complex phenomena that still need to be understood, mainly because of the strongly non-linear interactions and the presence of kinetic effects. In this context, investigating plasma dynamics is decisive for understanding fundamental processes occurring in different systems, ranging from very-far astrophysical objects to near-Earth environment and laboratory fusion devices. These systems routinely present a strongly nonlinear dynamics, which develops on a large range of spatial and time

† Email address for correspondence: oreste.pezzi@gssi.it

scales, including the ones associated with kinetic processes. In such systems, energy is typically injected at large fluid scales and cascades towards smaller scales, driving the system to cross three different physical regimes, ranging from fluid (MHD, Hall-MHD) to ion kinetic and eventually to electron kinetic scales. This multi-scale physics is the direct consequence of the weak plasma collisionality, that characterizes solar-wind and astrophysical plasmas (Kulsrud 2005; Califano & Mangeney 2008; Bruno & Carbone 2016) as well as fusion devices dynamics, where collisions can become effective at scales smaller than the electron kinetic scales (Falchetto et al. 2008).

As a result, the plasma is allowed to freely access the entire phase space and to manifest dynamical states far from thermal equilibrium (Valentini et al. 2005; Galeotti & Califano 2005; Marsch 2006; Franci et al. 2015; Servidio et al. 2015; Servidio et al. 2017; Franci et al. 2018; Sorriso-Valvo et al. 2018b; Pezzi et al. 2018; Cerri et al. 2018; Sorriso-Valvo et al. 2019). As an example, we highlight here the fundamental role of the collisionless magnetic reconnection, that –even within a fluid theory framework– drives a strongly nonlinear dynamics (at both ion and electron scales), without collisions to be relevant (Califano et al. 2007). Within this context, the Vlasov equation for each particle species, self-consistently coupled to Maxwell equations for fields, provides a complete description of the system dynamics, although in some cases the role of weak collisions should be also considered (Navarro et al. 2016; Pezzi et al. 2016, 2019). The Vlasov-Maxwell model is an nonlinear integro-differential set of equations in multi-dimensional phase space, whose analytic solutions are only available in a few simplified cases and in reduced phase-space geometry. A numerical approach is therefore mandatory to describe the dynamics of collisionless magnetized plasmas in fully nonlinear regime.

As of today, numerical simulations have provided significant insights on the plasma dynamics at proton and sub-proton spatial scales, where proton kinetic effects are dominant, while electrons can be approximated as an isothermal fluid (hybrid framework) (Valentini et al. 2007). In this range of scales, both Particle-In-Cell (PIC) and Eulerian hybrid codes have been extensively employed to investigate in detail a variety of physical phenomena such as, for instance, the development of the intermittent cascade of turbulent fluctuations (Parashar et al. 2009; Valentini et al. 2010; Servidio et al. 2012; Franci et al. 2015; Servidio et al. 2015; Franci et al. 2016; Valentini et al. 2016; Cerri et al. 2017; Cerri & Califano 2017; Valentini, F. et al. 2017; Pezzi et al. 2017b,a; Franci et al. 2018; Perrone et al. 2018; Cerri et al. 2018; Sorriso-Valvo et al. 2018a), the dynamo effect in turbulent plasmas (Rincon et al. 2016), the interaction of solar wind and Earth's magnetosphere at global scales (Palmroth et al. 2013; Kempf et al. 2013; Pokhotelov et al. 2013; Von Alfthan et al. 2014; Hoilijoki et al. 2016; Pfau-Kempf et al. 2018; Palmroth et al. 2018) and the dynamics of magnetic reconnection (Birn et al. 2001; Shay et al. 2001; Pritchett 2008; Califano et al. 2018). To reduce the computational cost of the simulation reduced models –such as the gyro-kinetics (Howes et al. 2006; Howes et al. 2008a,b; Schekochihin et al. 2008; Tatsuno et al. 2009; Howes et al. 2011; TenBarge et al. 2013; Told et al. 2015; Howes 2016) or the finite Larmor radius Landau fluid ones (Passot & Sulem 2007; Sulem & Passot 2015; Sulem et al. 2016; Kobayashi et al. 2017)– have been also widely adopted to describe plasma dynamics at kinetic scales.

Within the context of space plasmas, recent high-resolution observations conducted by the Magnetospheric Multi-Scale (MMS) mission (Burch et al. 2016; Fuselier et al. 2016) allowed, for the first time, to investigate the plasma dynamics at electron scale. The MMS mission focuses primarily on kinetic processes occurring in the electron diffusion region of magnetic reconnection (Burch et al. 2016; Torbert et al. 2016, 2018) and its

unprecedented high resolution observations confirm a very complex picture where several mechanisms can be at work in producing small-scale fluctuations (Le Contel et al. 2016; Breuillard et al. 2018; Chasapis et al. 2018). Magnetic reconnection often takes place within a turbulent environment where coherent structures –such as current sheets and X-points– naturally develop (Retinò et al. 2007; Servidio et al. 2009; Servidio et al. 2010; Haggerty et al. 2017; Phan et al. 2018). At the same time, plasma jets generated by magnetic reconnection can provide energy for sustaining the turbulence itself (Pucci et al. 2017; Cerri et al. 2017; Pucci et al. 2018). Reconnection is important for space and astrophysical plasmas as it is responsible for major plasma heating and particle acceleration in solar and stellar coronae, magnetars, accretion disks and astrophysical jets (Lyutikov 2003; Uzdensky 2011) as well as for tokamaks, being a major cause of loss of plasma confinement and plasma heating (Helander et al. 2002; Tanabe et al. 2015).

In order to properly combine and compare the experimental evidences at electron scales with theoretical investigations (Hesse et al. 2016), a huge numerical effort needs to be done yet. To this end, only few numerical algorithms which retain both proton and electron kinetic physics are nowadays available. Most of them are PIC codes (Markidis et al. 2010; Daughton et al. 2011; Zeiler et al. 2002; Camporeale & Burgess 2011; Karimabadi et al. 2013; Leonardis et al. 2013; Divin et al. 2015; Wan et al. 2015; Lapenta et al. 2015; Grošelj et al. 2017; Yang et al. 2017; Parashar et al. 2018; Shay et al. 2018; Lapenta et al. 2019; González et al. 2019), which capture the full dynamics (including electron scales) since their computational cost is smaller with respect to low-noise Eulerian (Vlasov) codes. However, at variance with noise-free Eulerian algorithms, PIC codes fail in providing a clean description of small-scale fluctuations (e.g., the electric field behavior around the X-point) and particle distribution functions in phase space, since they suffer from intrinsic statistical noise. Only very recently, the first attempts to describe plasma dynamics *via* Eulerian fully-kinetic codes have became affordable, thanks to the improved supercomputer capabilities (Schmitz & Grauer 2006a; Umeda et al. 2009, 2010; Tronci & Camporeale 2015; Delzanno 2015; Umeda & Wada 2016, 2017; Ghizzo et al. 2017; Juno et al. 2018; Roytershteyn et al. 2019; Skoutnev et al. 2019). As stated above, Eulerian algorithms generally require a computational cost significantly large as compared to PIC codes. A way to reduce the computational cost of a fully-kinetic Eulerian simulation consists in applying the so-called Darwin approximation (Kaufman & Rostler 1971; Birdsall & Langdon 2004; Schmitz & Grauer 2006a,b) to the Maxwell equations based on the expansion of the Maxwell system in the small parameter v^2/c^2 (Mangeney et al. 2002) (v being the typical plasma bulk speed). Within this approximation, all wave modes (including those triggered by charge separation) are retained except for light waves ($v_\phi \sim c$, v_ϕ being the wave phase speed); by doing so, the numerical stability condition for the timestep can be significantly relaxed.

In the present work we present a newly developed fully-kinetic Eulerian Vlasov-DArwin algorithm (ViDA) which integrates numerically the kinetic equations for a non-relativistic globally-neutral plasma composed of protons and electrons. Equations are discretized on a fixed-in-time grid in phase space with periodic boundary conditions in the physical domain. ViDA originates from the hybrid Vlasov-Maxwell code (Valentini et al. 2007) (hereafter referred as HVM code) and has been extended specifically to include electron kinetic dynamics. The paper is organized as follows. In Sect. 2 we revisit the Darwin approximation and describe the system of equations, that is numerically integrated through ViDA. We discuss in detail the strategy of the numerical integration of the Vlasov equation for each species and we show that the Darwin version of the Maxwell equations can be written as a set of Helmholtz and Poisson-like equations, solvable

through a spectral method. In the same Section, we also provide a description of the algorithm design. Then, in Sect. 3 we present first results obtained through this algorithm, concerning the propagation of i) electrostatic Langmuir waves, ii) whistler waves and iii) Alfvén waves. In Sect. 4, we describe the onset of the electron Weibel instability which is a plasma instability driven by the presence of a electron temperature anisotropy (Weibel 1959). In Sect. 5 we present preliminary results concerning one of the main potential applications of ViDA: the magnetic reconnection process at electron scales. Then, in Sect. 6, we discuss the performances of the algorithm. Finally, we conclude and summarize in Sect. 7.

2. The Vlasov-Darwin (VD) model

The Darwin approximation, that we briefly revisit in the current section, has been adopted to reduce the limitations on the timesteps for numerical integration (Kaufman & Rostler 1971; Mangeney et al. 2002; Birdsall & Langdon 2004; Schmitz & Grauer 2006a). Indeed, since Maxwell equations allow for the propagation of waves at the light speed c, the timestep Δt of any explicit numerical scheme solving these equations would be limited by the Courant-Friedrichs-Lewy (CFL) condition, $\Delta t \lesssim \Delta x/c$ (Peyret & Taylor 1986). The Darwin approximation, by dropping the transverse displacement current term, rules out the transverse light waves (i.e. the fastest waves in the system that propagate at phase speed c) and significantly relaxes the CFL condition.

We consider a non-relativistic, collisionless, fully-kinetic plasma composed by electrons and protons. The Vlasov-Darwin system of equations reads (in CGS units):

$$\partial_t f_\alpha + \boldsymbol{v}\cdot\nabla f_\alpha + \frac{Z_\alpha e}{m_\alpha}\left(\boldsymbol{E} + \frac{\boldsymbol{v}}{c}\times\boldsymbol{B}\right)\cdot\nabla_{\boldsymbol{v}} f_\alpha = 0 \tag{2.1}$$

$$\nabla\cdot\boldsymbol{E}_L = 4\pi\rho_c \tag{2.2}$$

$$\nabla\cdot\boldsymbol{B} = 0 \tag{2.3}$$

$$\nabla\times\boldsymbol{E}_T = -\frac{1}{c}\partial_t\boldsymbol{B} \tag{2.4}$$

$$\nabla\times\boldsymbol{B} = \frac{1}{c}\partial_t\boldsymbol{E}_L + \frac{4\pi}{c}\boldsymbol{j} \tag{2.5}$$

where $f_\alpha(\boldsymbol{x},\boldsymbol{v},t)$ is the distribution function (DF) of the $\alpha = p, e$ species, m_α and Z_α are respectively the mass and charge number of the α species and c is the light speed. ∂_t, ∇ and $\nabla_{\boldsymbol{v}}$ indicate the derivatives with respect to the time t, the spatial coordinates $\boldsymbol{x}$ and the velocity coordinates $\boldsymbol{v}$, respectively. $\boldsymbol{E}(\boldsymbol{x},t) = \boldsymbol{E}_L(\boldsymbol{x},t) + \boldsymbol{E}_T(\boldsymbol{x},t)$ and $\boldsymbol{B}(\boldsymbol{x},t)$ are the electric and magnetic field, respectively. The electric field has been decomposed into a longitudinal (irrotational, $\nabla\times\boldsymbol{E}_L = 0$) and a transverse (solenoidal, $\nabla\cdot\boldsymbol{E}_T = 0$) component (Griffiths 1962). According to the Darwin approximation, the transverse component of the displacement current has been neglected in the Ampere's law [Eq. (2.5)] (Birdsall & Langdon 2004; Schmitz & Grauer 2006a). The Darwin model, that retains at least the longitudinal component of the displacement current, is generally closer to the full Maxwell system with respect to models where the displacement current is completely neglected (Valentini et al. 2007; Tronci & Camporeale 2015).

The plasma charge density $\rho_c(\boldsymbol{x},t)$ and the current density $\boldsymbol{j}(\boldsymbol{x},t)$ are defined through

the first two velocity moments of the particle DFs:

$$\rho_c = e\sum_\alpha Z_\alpha n_\alpha = e\sum_\alpha Z_\alpha \int d\boldsymbol{v}\, f_\alpha \tag{2.6}$$

$$\boldsymbol{j} = \sum_\alpha \boldsymbol{j}_\alpha = e\sum_\alpha Z_\alpha n_\alpha \boldsymbol{V}_\alpha = e\sum_\alpha Z_\alpha \int d\boldsymbol{v}\, \boldsymbol{v}\, f_\alpha \tag{2.7}$$

Equations (2.1–2.5) can be further simplified to obtain a set of Helmholtz-like equations of state without explicit time derivatives (see Birdsall & Langdon (2004); Schmitz & Grauer (2006a) for details). By normalizing equations using a characteristic length $\bar{L}$, time $\bar{t}$, velocity $\bar{U} = \bar{L}/\bar{t}$, mass $\bar{m}$ and distribution function $f_{\alpha,0} = \bar{n}/\bar{U}^3$ (being $\bar{n} = \bar{L}^{-3}$ the equilibrium density), it is straightforward to get the dimensionless Vlasov-Darwin system of equations:

$$\partial_t f_\alpha + (\boldsymbol{v}\cdot\nabla) f_\alpha + \frac{Z_\alpha}{\mu_\alpha}(\boldsymbol{E} + \boldsymbol{v}\times\boldsymbol{B})\cdot\nabla_{\boldsymbol{v}} f_\alpha = 0 \tag{2.8}$$

$$\nabla^2\varphi = -\zeta^2\sum Z_\alpha n_\alpha \qquad \boldsymbol{E}_L = -\nabla\phi \tag{2.9}$$

$$\nabla^2\boldsymbol{B} = -\bar{u}^2\zeta^2\nabla\times\boldsymbol{j} \tag{2.10}$$

$$\nabla^2\hat{\boldsymbol{E}}_T - \bar{u}^2\zeta^2\sum_\alpha \frac{Z_\alpha^2 n_{\alpha,0}}{\mu_\alpha}\hat{\boldsymbol{E}}_T = \bar{u}^2\zeta^2\left[-\nabla\cdot\sum_\alpha Z_\alpha\langle\boldsymbol{v}\boldsymbol{v}\rangle_\alpha + \right.$$

$$\left. + \sum_\alpha \frac{Z_\alpha^2}{\mu_\alpha}(n_\alpha\boldsymbol{E}_L + \langle\boldsymbol{v}\rangle_\alpha\times\boldsymbol{B})\right] \tag{2.11}$$

$$\nabla^2\Theta = \nabla\cdot\hat{\boldsymbol{E}}_T \qquad \boldsymbol{E}_T = \hat{\boldsymbol{E}}_T - \nabla\Theta \tag{2.12}$$

$$\nabla\cdot\boldsymbol{B} = 0 \tag{2.13}$$

where $\langle h\rangle_\alpha = \int d\boldsymbol{v} f_\alpha h$. In Eqs. (2.8–2.13), the electric and magnetic fields are normalized to $\bar{E} = \bar{m}\bar{U}/e\bar{t}$ and $\bar{B} = \bar{m}c/e\bar{t}$, respectively. Note also that we set $k_B = 1$. Non-dimensional parameters are $\mu_\alpha = m_\alpha/\bar{m}$, $\bar{u} = \bar{U}/c$ and $\zeta = \bar{\omega}_p\bar{t}$, being $\bar{\omega}_p = \sqrt{4\pi e^2\bar{n}/\bar{m}}$. Note that in Eq. (2.11) we have omitted a term $\bar{u}^2\nabla\partial_{tt}\phi$ which could generate, in principle, an irrotational component, and we have introduced Eqs. (2.12) to preserve the solenoidality of $\boldsymbol{E}_T$ (Schmitz & Grauer 2006a). The spatial dependence of n_α on the left-hand side of Eq. (2.11) has been neglected ($n_\alpha \simeq n_{\alpha,0}$) to let coefficients be constant (Valentini et al. 2007).

2.1. *Conservation properties*

It is straightforward to verify that Eqs. (2.8–2.13) satisfy the mass $\int d\boldsymbol{x}d\boldsymbol{v} f_\alpha$ and entropy $S_\alpha = \int d\boldsymbol{x}d\boldsymbol{v} f_\alpha \log f_\alpha$ conservation. The energy conservation equation, obtained by multiplying Eq. (2.8) by $m_\alpha\boldsymbol{v}^2/2$, integrating over the phase-space volume $\int d\boldsymbol{x}d\boldsymbol{v}$ and summing over the species reads:

$$\mathcal{E}_{kin} + \mathcal{E}_{th} + \mathcal{E}_{mag} + \mathcal{E}_{el} = const \tag{2.14}$$

where the kinetic energy is $\mathcal{E}_{kin} = \sum_\alpha (m_\alpha/2)\int d\boldsymbol{x}\, n_\alpha \boldsymbol{u}_\alpha^2$, the thermal energy is $\mathcal{E}_{th} = \sum_\alpha (3/2)\int d\boldsymbol{x}\, n_\alpha T_\alpha$, the magnetic energy is $\mathcal{E}_{mag} = \sum_\alpha (\bar{m}/2\bar{u}^2\zeta^2)\int d\boldsymbol{x}\, \boldsymbol{B}^2$ and the electrostatic energy is $\mathcal{E}_{el} = \sum_\alpha (\bar{m}/2\zeta^2)\int d\boldsymbol{x}\, \boldsymbol{E}_L^2$. Note that the temperature of the α-species is defined as $3n_\alpha T_\alpha/m_\alpha = \int d\boldsymbol{v}(\boldsymbol{v}-\boldsymbol{u}_\alpha)^2 f_\alpha$ and, to get Eq. (2.14), we have used $\int d\boldsymbol{x}\, \boldsymbol{w}_T\cdot\boldsymbol{w}_L = 0$, $\boldsymbol{w}_T$ and $\boldsymbol{w}_L$ being a generic transverse and longitudinal vector, respectively. In each of the tests described in the present work we have checked the

conservation of these quantities: their variation with respect to initial values is always smaller than the 1%.

2.2. *ViDA algorithm and code design*

The Vlasov equation for each species is integrated numerically by employing the time splitting method first proposed by Cheng & Knorr (1976) in the electrostatic limit and later extended to the full electromagnetic case (Mangeney et al. 2002). Darwin equations are solved through standard Fast Fourier Transform (FFT) algorithms.

In our case, the splitting algorithm for Eq. (2.8) reads as follows:

$$\partial_t f_\alpha + (\boldsymbol{v}\cdot\nabla)\, f_\alpha = 0 \tag{2.15}$$

$$\partial_t f_\alpha + \frac{Z_\alpha}{\mu_\alpha}\,(\boldsymbol{E}+\boldsymbol{v}\times\boldsymbol{B})\cdot\nabla_{\boldsymbol{v}} f_\alpha = 0 \tag{2.16}$$

In the first equation $\boldsymbol{v}$ is a parameter, while in the second equation $\boldsymbol{x}$, $\boldsymbol{E}$ and $\boldsymbol{B}$ are parameters. At time t, the solutions of Eqs. (2.15–2.16) can be written as $\Lambda_{\boldsymbol{x}}(t)F_\alpha(\boldsymbol{x},\boldsymbol{v})$ and $\Lambda_{\boldsymbol{v}}F_\alpha(\boldsymbol{x},\boldsymbol{v})$, respectively. In last expressions, $\Lambda_{\boldsymbol{x}}$ and $\Lambda_{\boldsymbol{v}}$ are the advection operators in physical and velocity space, whose explicit definition, based on the third-order Van Leer scheme, can be found in Mangeney et al. (2002); while $F_\alpha(\boldsymbol{x},\boldsymbol{v}) = f_\alpha(\boldsymbol{x},\boldsymbol{v},t=0)$ is the initial condition. Note that $\Lambda_{\boldsymbol{v}}$ depends also on the particle species α and, for the sake of simplicity, we avoid to explicitly report such dependence.

The splitting scheme is a symplettic, second order accurate in time (see Mangeney et al. (2002) where the stability condition of the advection operator is also discussed) and the numerical solution at $t = t_N = N\Delta t$ is given by:

$$f_\alpha(\boldsymbol{x},\boldsymbol{v},t_N) = \left[\Lambda_{\boldsymbol{x}}\left(\frac{\Delta t}{2}\right)\Lambda_{\boldsymbol{v}}\left(\Delta t\right)\Lambda_{\boldsymbol{x}}\left(\frac{\Delta t}{2}\right)\right]^N f_\alpha(\boldsymbol{x},\boldsymbol{v},0) \tag{2.17}$$

At $t = 0$, the distribution function $F_\alpha(\boldsymbol{x},\boldsymbol{v}) = f_\alpha(\boldsymbol{x},\boldsymbol{v},t=0)$ is first advected in physical space by a half time-step, obtaining $\tilde{f}_\alpha(\boldsymbol{x},\boldsymbol{v},\Delta t/2)$. Then, the following structure is executed:

(i) Computing the moments of $\tilde{f}_\alpha$ and evaluating the electromagnetic fields $\boldsymbol{E}_L$, $\boldsymbol{E}_T$ and $\boldsymbol{B}$, at $t = \Delta t/2$, through Eqs. (2.9–2.13);

(ii) Performing a time-step advection in velocity space: $\hat{f}_\alpha = \Lambda_{\boldsymbol{v}}(\Delta t)\tilde{f}_\alpha$.

(iii) Performing a time-step advection in physical space: $\tilde{f}_\alpha = \Lambda_{\boldsymbol{x}}(\Delta t)\hat{f}_\alpha$.

This last structure is repeated in the algorithm, according to Eq. (2.17), in order to get the evolved distribution function at any time instant.

The phase space domain is discretized as follows. The physical space $D_{\boldsymbol{x}} = [0, L_x]\times[0, L_y]\times[0, L_z]$ is discretized with $N_x \times N_y \times N_z$ gridpoints and periodic boundary conditions are used. The velocity space $D_{\boldsymbol{v},\alpha} = [-v^{max}_{\alpha,x}, v^{max}_{\alpha,x}]\times[v^{max}_{\alpha,y}, v^{max}_{\alpha,y}]\times[-v^{max}_{\alpha,z}, v^{max}_{\alpha,z}]$ is discretized by $(2N_{\alpha,v_x}+1)\times(2N_{\alpha,v_y}+1)\times(2N_{\alpha,v_z}+1)$ grid points. Velocity-space boundary conditions impose $f_\alpha(|v_i| > v^{max}_{\alpha,i}) = 0$ $(i = x, y, z)$. In order to ensure mass conservation, $v^{max}_{\alpha,i}$ is typically set to be a large multiple of the thermal speed $v_{th,\alpha} = \sqrt{T_\alpha/m_\alpha}$.

The ViDA algorithm has been designed in such a way that the user can select (i) different normalizations of the model equations, (ii) the possibility of setting motionless protons and (iii) different dimensionalities of the physical-space domain ($1D$, $2D$, or $3D$), the velocity-space domain being always three-dimensional ($3V$). Within ViDA spatial vectors always have three components and can be function of one, two or three spatial variables, depending on the physical-space dimensionality. Since Darwin equations are a set of Helmholtz-like equations, initial perturbations have to be introduced through the

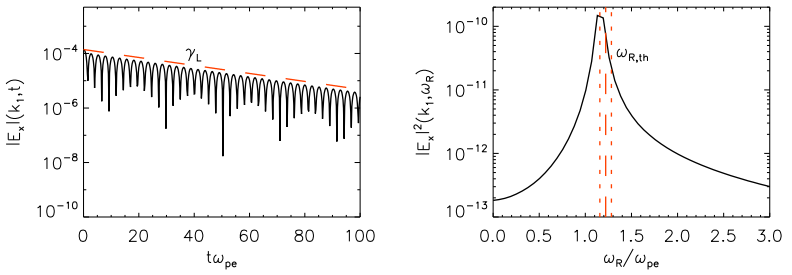

FIGURE 1. Left: Time evolution of $|E_x|(k_1, t)$. The red dashed line indicates the predicted Landau damping rate γ_L. Right: Energy peak $|E_x|^2(k_1, \omega_R)$ as a function of the pulsation ω_R. The red dashed line indicates the theoretical wave frequency $\omega_{R,th}$, while red dot-dashed lines show the ω_R–resolution, i.e. $\omega_{R,th} \pm \Delta\omega_R/2$. The theoretical expectations for the Langmuir wave damping and the pulsation have been obtained with a numerical solver of the linear dispersion relation.

particle DFs (and their moments): this represents a difference with respect to standard codes where also magnetic perturbations can be introduced. A check on the solenoidality of $\boldsymbol{B}$ and $\boldsymbol{E}_T$ is also implemented at each time step.

The computational effort necessary to solve VD equations is significant and a massive parallelization, based on both MPI and OpenMP paradigms is implemented. The MPI paradigm, first introduced for the VDF by Mangeney et al. (2002), is adopted to parallelize the physical-space computational domain for both particle DFs (and their moments) and electromagnetic field. Hence each MPI thread accesses a finite portion of phase space, composed by a sub-portion of physical space and by the whole velocity space. Within each MPI thread, the OpenMP directives are adopted to parallelize the velocity-space cycles. The parallelization of the electromagnetic field is a new feature recently introduced in the HVM code in Cerri & Califano (2017) and it is essential to perform high-resolution Eulerian Vlasov simulations, in particular in $3D$. Preliminary tests on performance and scalability are reported in Sect. 6.

2.3. *Normalizations of the Vlasov-Darwin equations*

In order to normalize Eqs. (2.8–2.13), three possible choices have been implemented in ViDA:

(i) *Electrostatic* normalization. Characteristic quantities are: length $\bar{L} = \lambda_{D,e}$, time $\bar{t} = \omega_{p,e}^{-1}$, velocity $\bar{U} = v_{th,e}$ and mass $\bar{m} = m_e$. Here $\lambda_{D,e} = \sqrt{T_e/4\pi n_e e^2}$, $\omega_{p,e} = (\sqrt{4\pi n_e e^2/m_e})^{-1}$, $v_{th,e} = \sqrt{T_e/m_e} = \lambda_{D,e}\omega_{p,e}$ and m_e are the electron Debye length, the electron plasma frequency, the electron thermal speed and the electron mass, respectively. This normalization is appropriate for describing phenomena occurring at electron scales, such as the propagation of electrostatic plasma waves.

(ii) *Electromagnetic* normalization. Characteristic quantities are: length $\bar{L} = d_e$, time $\bar{t} = \omega_{p,e}^{-1}$, velocity $\bar{U} = c$ and mass $\bar{m} = m_e$, where $d_e = c/\omega_{p,e}$ is the electron skin depth. This normalization can be adopted for describing electromagnetic phenomena, where both protons and electrons are involved, such as magnetic reconnection and plasma turbulence at kinetic scales.

(iii) *Hybrid* normalization. Characteristic quantities are: length $\bar{L} = d_p$, time $\bar{t} = \Omega_{c,p}^{-1}$, velocity $\bar{U} = v_A$ and mass $\bar{m} = m_p$. In previous expressions $\Omega_{cp} = eB_0/m_p c$, $v_A = B_0/\sqrt{4\pi n_p m_p}$, $d_p = v_A/\Omega_{cp}$ and m_p are the proton cyclotron frequency, the proton Alfvén speed, the proton skin depth and the proton mass, respectively. This normalization

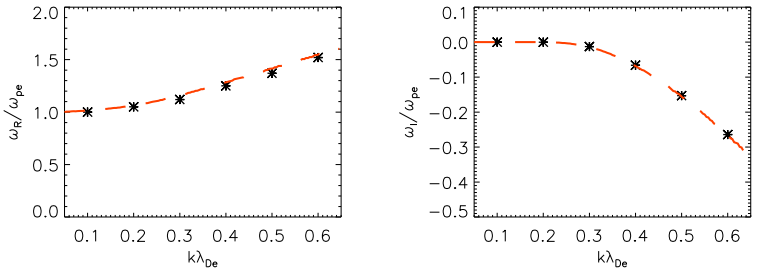

FIGURE 2. Pulsation ω_R (left) and damping rate γ_I (right), in units of $\omega_{p,e}$, from the simulation (black dots) and from the linear numerical solver (red dashed line) as a function of the wave number $k\lambda_{D,e}$.

is useful for investigating the turbulent cascade in the sub-proton range, where electron physics starts to play a role.
These three normalizations can be adopted to describe, in a more natural way (i.e. characteristic scales close to unity), phenomena where electrostatic, electromagnetic, or proton inertial effects dominate, respectively.

3. Numerical tests of ViDA

In this section we report the results of several tests performed to evaluate the capabilities of ViDA in describing basic collisionless plasma physics dynamics. The proper behavior and reliability of the code has been tested against the propagation of Langmuir waves, in both linear and nonlinear regime, whistler waves and Alfvén waves.

3.1. *Propagation and damping of Langmuir waves*

For these tests we adopted the *electrostatic* normalization. We discuss results of simulations performed with motionless protons in $1D$–$3V$ phase-space configuration, where Langmuir waves propagate along the x direction. Physical and velocity space have been discretized with $N_x = 128$ and $N_{e,v_x} = 50$, $N_{e,v_y} = N_{e,v_z} = 15$ grid points, respectively. In the case of mobile protons ($m_p/m_e = 1836$ and $T_p/T_e = 1$), the propagation of Langmuir waves has been reproduced with lower phase space resolution, but the results are quantitatively similar to those discussed in the following. We have also separately tested the propagation of Langmuir waves along y and z directions by carrying out $2D$–$3V$ and $3D$–$3V$ runs.

The initial equilibrium is given by an electron Maxwellian distribution spatially homogeneous. The plasma is unmagnetized, the initial electron temperature is $T_e = 1$ (in scaled units). At $t = 0$, the electron number density is perturbed through a sinusoidal perturbation $\delta n_e/n_{e,0} = A\sin(kx)$, $A = 10^{-4}$ and $k = k_1 = 2\pi/L$ being the amplitude and the wave-number, respectively. The box length is $L = 18\lambda_{D,e}$ ($k_1 = 0.35$) and $v_{e,i}^{max} = 5v_{th,e}$ ($i = x, y, z$). The system evolution is reproduced up to a maximum time $t_{max} = 100\omega_{p,e}^{-1}$, while the numerical recurrence time is $t_{rec} = 2\pi/k\Delta v \simeq 180\omega_{p,e}^{-1}$(Cheng & Knorr 1976; Galeotti et al. 2006; Pezzi et al. 2016).

The left panel of Fig. 1 shows the time evolution of the amplitude of the $k_x = k_1$ Fourier component of the electric field $|E_x|(k_1, t)$, in a semi-logarithmic plot. The electric field undergoes Landau damping (Landau 1946); the observed damping rate shows a very good agreement with the theoretical prediction $\gamma_L = -3.37 \times 10^{-2}\omega_{p,e}$ (red-dashed line), evaluated through a numerical linear solver for the roots of the electrostatic Vlasov

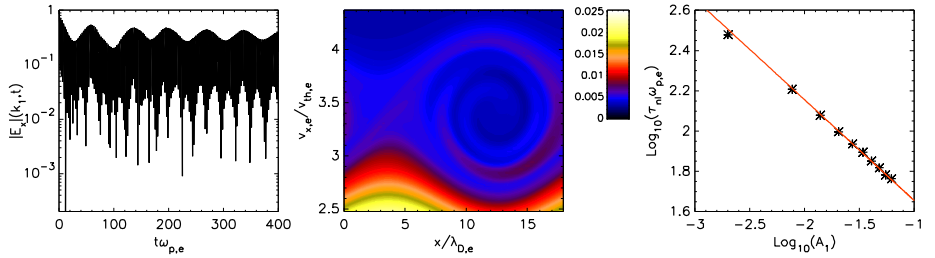

FIGURE 3. Left: Time evolution of $|E_x(k_1,t)|$ for the simulation with $A = 8 \times 10^{-2}$. Center: Contour plot of $\tilde{f}_e(x,v_x) = \int dv_y dv_z f_e(x,\boldsymbol{v})$ in the plan x–v_x. Right: Nonlinear time τ_{nl} as a function of the first peak amplitude A_1. The red line reports the predicted scaling ~ -0.5 (the result of the linear fit is ~ -0.48).

dielectric function. In the right panel of Fig. 1 we report the resonant curve, obtained by Fourier transforming the electric signal in space and time; we plot the spectral electric energy $|E_x|^2(k_1,\omega_R)$ as a function of the pulsation ω_R. As expected, the resonant curve displays a well-defined frequency peak in correspondence of a value of the pulsation $\omega_R = 1.22\omega_{p,e}$. In the right panel of the figure, the vertical red-dashed line represents the value of the theoretical resonant pulsation $\omega_{R,th}$ obtained through the linear solver, while the two vertical red-dot-dashed lines indicate the interval of uncertainty of the numerical code, due to the time discretization $\Delta\omega_R = 2\pi/t_{max} \simeq 0.063\omega_{p,e}$. Again, numerical results are in very good agreement with theoretical predictions.

In order to show the dependence of real ω_R and imaginary ω_I part of the frequency as a function of the wavenumber, we have performed an additional $1D$–$3V$ run, in which the initial perturbation is a superposition of the first six wavenumbers $k_x = [k_1, 6k_1]$, where $k_1 = 2\pi/L$ ($L = 2\pi 10\lambda_{D,e}$); the other parameters are the same as in the previous run. To avoid numerical recurrence, phase space has been discretized with $N_x = 128$, $N_{e,v_x} = 100$ and $N_{e,v_y} = N_{e,v_z} = 15$. Figure 2 reports by stars the dependence of ω_R (left) and ω_I (right), in units of ω_{pe}, as a function of the wave number $k\lambda_{D,e}$. A very good agreement with theoretical expectations (red-dashed curves) is recovered for both real and imaginary parts of the complex frequency.

We conclude this section by focusing on the nonlinear regime of the Langmuir wave dynamics (see, for example, Brunetti et al. (2000) and refs. therein). We have performed ten different runs, varying the amplitude of the initial density perturbation in the range $A = [8 \times 10^{-3}, 8 \times 10^{-2}]$. In this case, phase space has been discretized with $N_x = 128$, $N_{e,v_x} = 150$ and $N_{e,v_y} = N_{e,v_z} = 15$, while $t_{max} = 400\omega_{pe}^{-1}$. The box length is $L_x = 18\lambda_{D,e}$, while $v_{e,i}^{max} = 5v_{th,e}$ ($i = x,y,z$). As reported in the left panel of Fig. 3, the time evolution of the electric-field Fourier component shows an early linear damping phase (Landau 1946), until particle trapping arrests the damping and produces oscillations of the signal envelope (O'Neil 1965). At large times, a phase-space vortex is observed in the electron DF in the vicinity of the wave phase speed, as reported in the center panel of Fig. 3(center). As it has been shown in O'Neil (1965), the nonlinear trapping time τ_{nl} depends on the saturation amplitude A_1 of the electric oscillations as $\tau_{nl} \sim A_1^{-1/2}$. For each of the ten simulations, we evaluated A_1 and τ_{nl} at the time of the first peak of the electric envelope oscillations. The right panel of Fig. 3 shows in log-log plot τ_{nl} as a function of A_1 (stars), compared to the theoretical expectation (red line), showing a very nice agreement.

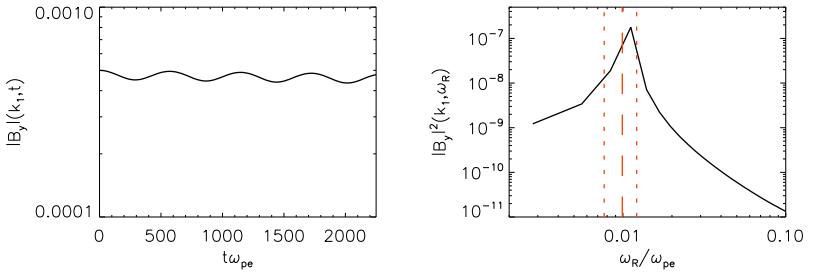

FIGURE 4. Left: Time evolution of $|B_y|(k_1, t)$. Right: Spectral magnetic energy $|B_y|^2(k_1, \omega_R)$ as a function of the pulsation ω_R. The red dashed line indicates the theoretical wave frequency $= \omega_{R,th}$, while red dot-dashed lines show the ω_R-resolution $\omega_{R,th} \pm \Delta\omega_R/2$.

3.2. *Propagation of whistler waves*

To reproduce the propagation of whistler waves at electron scales, the *electromagnetic* normalization has been employed. Protons are assumed just as a fixed neutralizing background. Again, we have verified that the ViDA code behaves exactly in the same manner in the three spatial directions. Hence, we discuss here the result of a $1D$–$3V$ run, where $\boldsymbol{B}_0 = B_0 \boldsymbol{e}_x$ ($B_0 = 1$) and protons are not fixed. The box length is $L_x = 2\pi 10 d_e$, while $v_{e,i}^{max} = 10 v_{th,e}$ and $v_{p,i}^{max} = 7 v_{th,p}$ ($i = x, y, z$). Note that increasing the value of $v_{p(e)}^{max}$ has been necessary to ensure mass conservation. The phase space has been discretized with $N_x = 128$, $N_{e,v_x} = N_{e,v_y} = N_{e,v_z} = 50$ and $N_{p,v_x} = N_{p,v_y} = N_{p,v_z} = 35$. We also set $m_p/m_e = 1836$, $T_e/T_p = 1$, $\bar{u} = v_{th,e}/c = 10^{-3}$ and $\zeta = 1$.

The equilibrium is composed of Maxwellian velocity distributions for both protons and electrons and homogeneous density. The initial equilibrium is then perturbed with the following electron bulk-speed perturbations:

$$\delta u_{e,y} = A \sin(kx) \tag{3.1}$$

$$\delta u_{e,z} = A \cos(kx) \tag{3.2}$$

where $A = 10^{-3}$ and $k = k_1 = 2\pi/L_x$.

By solving Darwin equations, these perturbations generate a current density and then magnetic fluctuations. Figure 4 reports the time evolution of $|B_y|(k_1, t)$ (left) and the frequency peak of the spectral magnetic energy $|B_y|^2(k_1, \omega_R)$ as a function of the pulsation ω_R (right). The magnetic field clearly oscillates at the correct frequency $\omega_{R,th} = 0.91\omega_{p,e}$, that can be evaluated from the linear dispersion relation for whistler waves (obtained by assuming motionless protons and cold electrons): $\omega_{R,th}(k) = B_0 k^2/(1 + k^2)$ (Krall & Trivelpiece 1973). Note that, for the considered wave-number, a negligible damping of whistler waves is expected. In the left panel of Fig. 4, red-dashed line represents the value of the resonant pulsation from above expression for $\omega_{R,th}$, while the two vertical red dot-dashed lines indicate the interval of numerical uncertainty $\Delta\omega_R = 2\pi/t_{max} \simeq 0.063\omega_{p,e}$.

3.3. *Propagation of Alfvén waves*

Here we show numerical results concerning the propagation of Alfvén waves along a background magnetic field. The adopted normalization for these tests is the *hybrid* one. We perform a $1D$–$3V$ run, where $\boldsymbol{B}_0 = B_0 \boldsymbol{e}_x$ and $B_0 = 1$. The box length is $L_x = 2\pi 50 d_p$, while $v_{e,i}^{max} = 5 v_{th,e}$ and $v_{p,i}^{max} = 5 v_{th,p}$ ($i = x, y, z$). The phase space has been discretized with $N_x = 32$, $N_{e,v_x} = N_{e,v_y} = N_{e,v_z} = 25$, $N_{p,v_x} = 40$, and $N_{p,v_y} = N_{p,v_z} = 35$

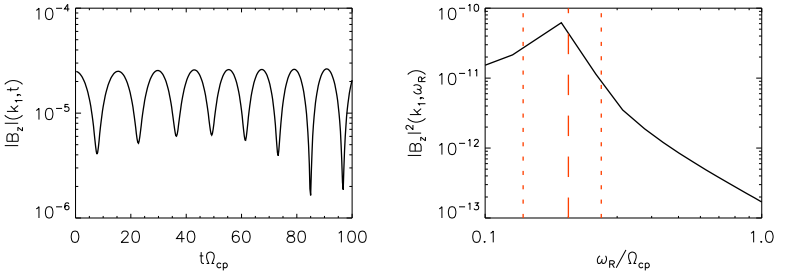

FIGURE 5. Left: Time evolution of $|B_z|(k_1, t)$. Right: Magnetic spectral energy $|B_z|^2(k_1, \omega_R)$ as a function of ω_R. The red solid line indicates the theoretical wave frequency $\omega_{R,th}$, while red dashed lines show the ω_R-resolution $\omega_{R,th} \pm \Delta\omega_R/2$.

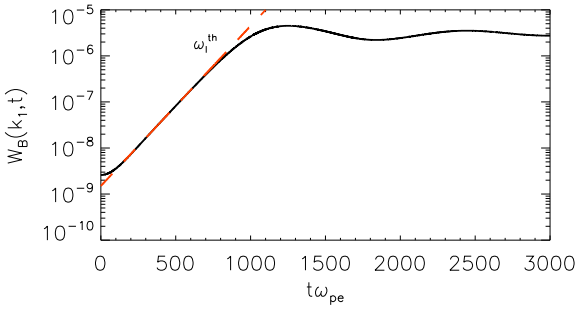

FIGURE 6. Time evolution of $W_B(k_1) = (|B_y|^2(k_1) + |B_z|^2(k_1))/2$. The red dashed line indicates the linear instability growth $\omega_I^{th} \simeq 4\times10^{-3}\omega_{p,e}$, calculated with a linear solver of the fully-kinetic dispersion relation (Camporeale & Burgess 2017).

gridpoints. The mass ratio has been artificially set $m_p/m_e = 25$, thus avoiding extremely small timesteps, while $T_e/T_p = 1$, $\bar{u} = v_A/c = 10^{-3}$ and $\zeta = c/v_A = 10^3$. Initial proton β_p is $\beta_p = 2v_{th,p}^2/v_A^2 = 1$.

The initial equilibrium, composed of spatially homogeneous Maxwellian protons and electrons, has been perturbed with the following proton bulk-speed perturbations:

$$\delta u_{p,y} = A\sin(kx) \tag{3.3}$$
$$\delta u_{p,z} = A\cos(kx) \tag{3.4}$$

where $A = 10^{-4}$ and $k = k_1 = 2\pi/L_x$. Figure 5 shows the time evolution of $|B_z|(k_1, t)$ (left) and the magnetic spectral energy $|B_z|^2(k_1, \omega_R)$ as a function of ω_R (right). The recovered resonant peak is in agreement with the theoretical pulsation, evaluated through a fully-kinetic linear solver of the dispersion relation (Camporeale & Burgess 2017). Moreover, no Landau damping is observed, since it occurs at much smaller scales (Barnes 1966; Vàsconez et al. 2014; Camporeale & Burgess 2017). This test represents the first attempt towards a general description of Alfvén waves, where electron physics is also taken into account. Since including electron physics is currently too computational demanding, we plan to continue the investigation in a separate, future work.

4. Temperature anisotropy driven instability: electron Weibel instability

Another class of interesting numerical tests, which can be performed to point out the reliability of the ViDA code, concerns the onset of micro-instabilities, such as whistler, mirror and Weibel instabilities driven by a temperature anisotropy (Weibel 1959; Gary & Karimabadi 2006; Califano et al. 2008; Palodhi et al. 2009, 2010; Chen & Chacón 2014, 2015; Camporeale & Zimbardo 2015).

Here we focus on the development of the electron Weibel instability, that produces electromagnetic fluctuations transverse to the wavevector $\boldsymbol{k}$. The most suitable normalization to perform this analysis is the *electromagnetic* one. In particular we discuss the results of a 1D–3V run with $\boldsymbol{k} = k\hat{\boldsymbol{e}}_x$, although we have verified that instability is triggered in the same way also in the different phase space configuration ($2D$ and $3D$). The mass ratio is $m_p/m_e = 100$, while $T_e/T_p = 0.01$. Electrons are initialized with a bi-Maxwellian distribution function, with thermal speeds $v_{th,e,x} = 2.5 \times 10^{-2}c$ and $v_{th,e,y} = v_{th,e,z} = 4 \times 10^{-2}c$, this giving a temperature anisotropy $A = T_{y(z)}/T_x = 2.56$. Protons have a Maxwellian velocity distribution at $t = 0$, with a thermal speed $v_{th,p} = v_{th,e,x}$ and homogeneous density. However, in this case, protons mainly act just as a neutralizing background, not being involved in the dynamics during the linear stage (i.e. during the instability development). No background magnetic field has been introduced. Physical space, whose length is $L_x = 32d_e$, has been discretized with $N_x = 64$ gridpoints. Velocity space has been discretized with 51^3 gridpoints for both protons and electrons and $v_{e(p)}^{max} = 5v_{th,e(p)}$ in each velocity directions.

The initial equilibrium has been perturbed through a sinusoidal, transverse perturbation, imposed on the electron bulk speed:

$$\delta u_{e,y} = Asin(kx) \tag{4.1}$$

$$\delta u_{e,z} = Acos(kx) \tag{4.2}$$

where $A = 2 \times 10^{-5}$ and $k = k_1 = 2\pi/L_x$. Such bulk-speed perturbations produce a current density, which in turn generates magnetic fluctuations. Figure 6 reports the time evolution of the magnetic spectral energy density $W_B(k_1, t) = (|B_y|^2(k_1, t) + |B_z|^2(k_1, t))/2$. The red-dashed line indicates the expected linear instability growth rate $\omega_I^{th} \simeq 4 \times 10^{-3}\omega_{p,e}$, evaluated through a linear solver for the roots of the kinetic electromagnetic dielectric function. In the early stage of the simulation, W_B increases exponentially with a growth rate in very good agreement with the expected one. Then, oscillations saturate at a nearly constant value in the nonlinear regime of evolution (Chen & Chacón 2014).

5. Dynamics of magnetic reconnection

In this Section we present the results of a magnetic reconnection simulation. Generally speaking, Vlasov simulations of magnetic reconnection represent a strong numerical challenge because of the huge memory and CPU time required by Eulerian algorithms. This approach, if successful, would certainly provide a crucial contribution to the understanding of the magnetic reconnection process especially at electron scales, thanks to the fact that Eulerian algorithms allow for an almost noise-free description of fields and particle DFs. A noise-free description is crucial to properly understand e.g. which electromagnetic fluctuations contribute to the reconnection electric field in the form of

anomalous resistivity and how distribution functions are modified leading to electron heating.

We have performed a $2D$–$3V$ symmetric magnetic reconnection simulation. Reconnection is symmetric when the values of magnetic field and density are equal on the two opposite sides of the current sheet. The initial condition of our simulation is the one adopted in the GEM challenge (Birn et al. 2001), in order to allow for a direct comparison to previous studies (Birn et al. 2001; Schmitz & Grauer 2006b). For this reason, we have also chosen the *hybrid* normalization (see Sect. 2.3).

The equilibrium is set by adapting the Harris equilibrium (Harris 1962) to the periodic boundary conditions in the spatial domain. In particular, the component of the magnetic field $B_x(y)$ corresponding to the double current sheet profile reads:

$$B_x(y) = B_0\left[\tanh\left(\frac{y - L_y/2}{L_1}\right) - \tanh\left(\frac{y}{L_2}\right) - \tanh\left(\frac{y - L_y}{L_2}\right)\right]. \tag{5.1}$$

This profile is characterized by the presence of two gradients (the current sheets) varying as an hyperbolic tangent and located at $y = L_y/2$ and $y = 0$ (and so at $y = L_y$) where L_y is the length of the spatial domain in the y direction. The first hyperbolic tangent is the one defined in Harris (1962) and L_1 is the corresponding current sheet thickness. The second and third hyperbolic tangent in Eq.(5.1) have been included to satisfy the spatial periodicity; the value of L_2 is taken sufficiently large compared to L_1 to slow down the development of reconnection in the second current sheet with respect to the main one. The electron and ion temperature are set uniform at the initial time and the density $n(y)$ is defined in order to satisfy pressure balance. Then, from Eq. (2.5) and considering $\partial_t \mathbf{E}_L = 0$ at the initial time, we get the initial current density $\mathbf{j} = (0,\ 0,\ j_z(y))$.

Following the prescriptions of the Harris equilibrium we get, in normalized units,

$$n_0(T_e + T_p) = \frac{B_0^2}{2} \tag{5.2}$$

$$\frac{u_{e,0}}{T_e} = -\frac{u_{p,0}}{T_p} \tag{5.3}$$

$$\frac{j_z(y)}{n(y)} \equiv u_0 = u_{p,0} - u_{e,0} \tag{5.4}$$

Eq. (5.3) corresponds to the no charge separation condition of the Harris equilibrium so that quasi-neutrality is imposed, $n_e(y) = n_p(y) = n(y)$. In other words, the electric field is zero at the initial time. Moreover, from Eqs.(5.3)–(5.4) we have:

$$u_{e,0} = -\frac{u_0}{1 + T_p/T_e} \tag{5.5}$$

$$u_{p,0} = \frac{u_0}{1 + T_e/T_p} \tag{5.6}$$

It is worth to point out that this is not an exact Vlasov kinetic equilibrium. In particular, it differs from the equilibrium presented by Harris since in this simulation the spatial domain is periodic in the varying y-direction. On the other hand, the initial configuration is in force balance and we have checked that the initial equilibrium is not significantly affected by, for example, ballistic effects within the time scale of reconnection considered here. As for the GEM challenge (Birn et al. 2001), fluctuations are superposed to the initial magnetic field in order to obtain a single magnetic island at the center of the

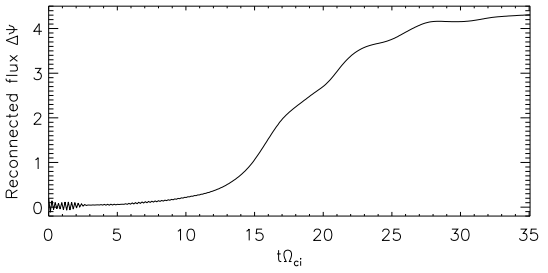

FIGURE 7. Time evolution of the reconnected magnetic flux $\Delta\psi$.

space domain at the initial time. In particular, $\delta\mathbf{B} = \nabla\delta\psi \times \hat{z}$ and

$$\delta\psi(x,y) = \psi_0 \cos(2\pi x/L_x)\cos(2\pi y/L_y) \tag{5.7}$$

where, as already stated, L_x and L_y are the lengths of the spatial domain in x and y direction respectively. According to GEM challenge, in scaled units, ψ_0 is set to 0.1.

By using the relation $\delta\mathbf{B}(x,y) = \nabla\delta\psi(x,y) \times \hat{z}$ and Eq.(2.10), we derive the expression for the current density fluctuations $\delta\mathbf{j}(x,y)$ consistent with $\delta\psi(x,y)$. In particular, it is possible to define $\delta\mathbf{j}(x,y) = (0,0,\delta j_z(x,y))$. Finally, the initial electron and proton distribution functions are shifted Maxwellian distributions with drift velocities along the z direction and temperature T_e and T_p.

The phase space has been discretized with $N_x \times N_y = 512 \times 512$ gridpoints in the spatial domain, $N_{e,v_x} \times N_{e,v_y} \times N_{e,v_z} = 41 \times 41 \times 81$ gridpoints in the velocity domain for electrons and $N_{p,v_x} \times N_{p,v_y} \times N_{p,v_z} = 31 \times 31 \times 31$ gridpoints in the velocity domain for protons. We also set $v_e^{max} = 5\ v_{th,e}$ and $v_p^{max} = 5\ v_{th,p}$, where the normalized $v_{th,p}$ is set to 1. Other simulation parameters are $L_1 = 0.5d_p$, $L_2 = 2.5d_p$, $m_p/m_e = 25$, $n_\infty = 0.2$, $T_e/T_p = 0.2$, $L_x = L_y = 25.6d_p$. Also, we set $B_0 = 1$ and $n_0 = 1$. All parameters are chosen to be as close as possible to the simulation parameters listed in Birn et al. (2001).

In Figure 7 we show the evolution of the reconnected flux given by the difference $\Delta\psi$ between the magnetic flux ψ evaluated at the X point and at the O point. Accordingly to the initial perturbation, the X and the O point are initially located at $(L_x/2, L_y/2)$ and $(0, L_y/2)$ and their location does not significantly change throughout the simulation run. The behavior of $\Delta\psi$ is very similar to the evolution of the reconnected flux in Ref. (Birn et al. 2001). Reconnection evolves with a reconnected flux that remains close to zero until $t \sim 15\ \Omega_{c,p}^{-1}$, when a sharp increase is observed. Then, the reconnection rate stays relatively constant until the reconnected flux begins to saturate at $t \sim 30\ \Omega_{c,p}^{-1}$.

In Figure 8 we show the contour plots of the out of plane magnetic field B_z (a), of the electron current density in the z-direction $j_{e,z}$ (b), of the proton current density in the z-direction $j_{p,z}$ (c) and of the electron number density n_e (d). In each panel, the contour lines of the magnetic flux ψ are superposed. B_z exhibits the typical Hall quadrupolar pattern usually observed during symmetric magnetic reconnection. This magnetic signature indicates that the ions are demagnetized while the electrons are still frozen to the magnetic field. The difference in their dynamics produces the out-of-plane B_z (Mandt et al. 1994; Uzdensky & Kulsrud 2006). The quadrupolar structure that we find is analogous to the one obtained with other kinetic codes, both Eulerian (Schmitz & Grauer 2006b, see Fig. 2) and Lagrangian (Pritchett 2001, see Plate 1(b)). We note that the $j_{p,z}$ pattern closely follows the density pattern ($n_e \simeq n_p$) so that $j_{p,z}$ is depleted at the X point while it reaches its maximum value within the magnetic island. On the other hand, $j_{e,z}$ is enhanced at the X point and the region of strong $j_{e,z}$ is

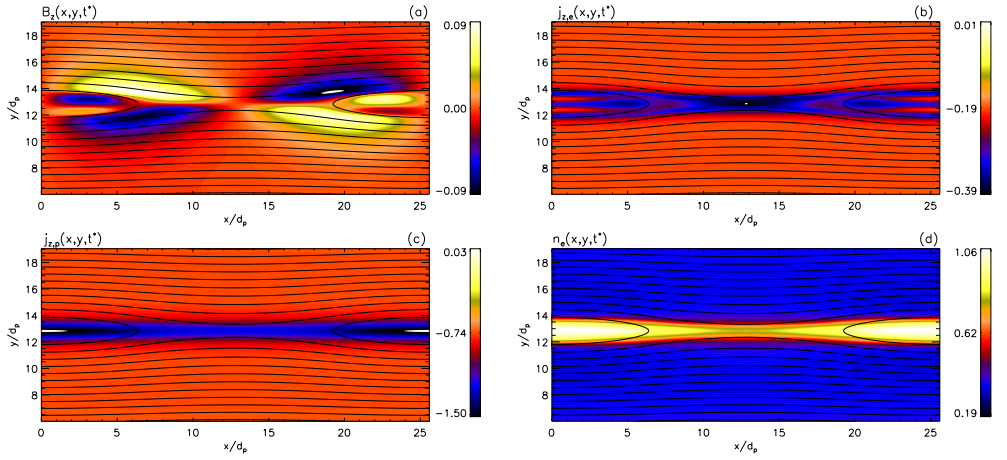

FIGURE 8. Contour plots of B_z (a); out-of-plane electron current density $j_{e,z}$ (b); out-of-plane proton current density $j_{p,z}$ (c); and electron number density n_e (d). The quantities are shown at the time $t^* = 15.27\ \Omega_{c,p}^{-1}$. At that time $\Delta\psi = 1.18$. All the panels are zoomed in y in the interval $[6\ d_p, 19\ d_p]$.

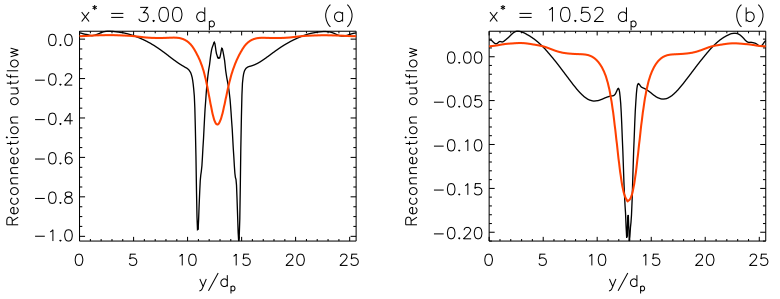

FIGURE 9. (a) x component of the electron velocity u_e (black line) and of the proton velocity u_p (red line) at $x^* = 3.00\ d_p$ and (b) at $x^* = 10.52\ d_p$. The quantities are shown at the time $t^* = 18.13\ \Omega_{c,p}^{-1}$.

elongated along x. Away from the X point, $j_{e,z}$ splits into two branches that identify the separatrices, as it was also observed by Shay et al. (2001) (see Fig.6(d)). The electron current at the X line has a thickness comparable to d_p which corresponds to 5 d_e. The maximum value of the normalized B_z is 0.09 while the maximum values of $j_{p,z}$ and $j_{e,z}$ are 0.39 and 1.49, respectively. These values are overall slightly smaller than the values found in a similar Vlasov-Darwin simulation described in Ref. (Schmitz & Grauer 2006b).

In Figure 9 we show the reconnection outflow of protons and electrons at $t^* = 18.13\ \Omega_{c,p}$. In particular, we note that at $x = 3\ d_p$ (panel (a)), corresponding to a distance of 9.8 d_p from the X-point located at $L_x/2 = 12.8\ d_p$, the electron velocity is characterized by two peaks corresponding to the separatrices, while the proton velocity is concentrated in the center of the outflow region and it reaches lower values, as expected. The presence of the two peaks is consistent with the $j_{e,z}$ pattern shown in Fig. 8(b). Fig. 9(b) shows the same quantities of Fig.9(a) at a distance of 2.3 d_p from the X-point where the outflow is still developing and we note that $u_{e,x}$ is rather similar in shape and value to $u_{p,x}$.

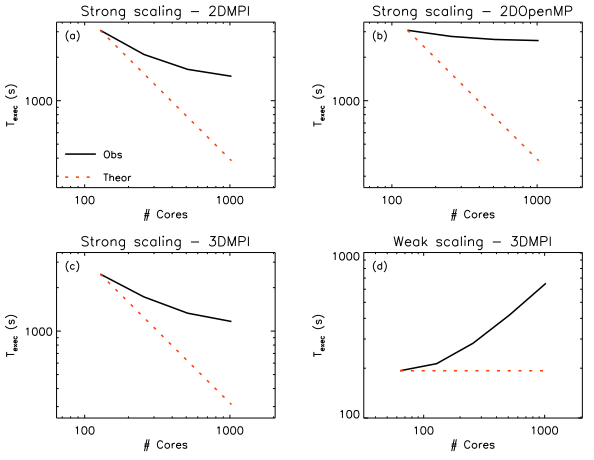

FIGURE 10. (a) Strong scaling from 128 to 1024 cores on Marconi KNL using 2 OpenMP threads per Task MPI on the 2.5D setup. (b) Strong scaling using 64 MPI task and from 2 to 16 OpenMP Threads per task on the 2.5D setup. (c) Strong scaling from 128 to 1024 cores on Marconi KNL using 2 OpenMP threads per Task MPI on the 3D setup. (d) Weak scaling from 64 to 1024 cores on Marconi KNL using 2 OpenMP threads per Task MPI on the 3D setup.

6. Performance test on the ViDA code

In this section, we present preliminary performance tests of ViDA implemented on the Marconi-KNL cluster at the CINECA supercomputing center (Casalecchio di Reno (BO), Italy). The Marconi cluster is equipped with 3600 Lenovo Adam Pass nodes, interconnected through the Intel OmniPath network and each one composed by 1KNL processor (68 cores, 1.40GHz), formally 96 GB of RAM (effective 83 GB) and 16 GB of MCDRAM. The tests have been performed on a simple equilibrium configuration (Maxwellian DFs with no perturbations). We remark however that this choice does not affect the code performance.

ViDA numerically integrates VD equations in a six-dimensional phase-space ($3D$–$3V$: x, y, z, v_x, v_y, v_z). Only the $3D$ physical space is parallelized using cubic cells (squared in the $2D$ configuration). For implementing these tests, we have chosen 51^3 velocity gridpoints for each particle VDF (protons and electrons), which represent a typical value adopted in production runs, and we have performed about 100 timesteps per test (note that changing the step number does not act on the code scalability). Note that two VDFs are advanced in time through the ViDA algorithm, this limiting the number of spatial grid points per single processor and hence increasing the number of communications.

As a first step, we have analyzed the parallel performance in the $2D$–$3V$ configuration, adopting a physical-space grid with 1024×1024 points. This setup requires about 6 TB of RAM, corresponding to, at least, 64 Marconi-KNL nodes. We have performed a strong scaling test by reducing the number of MPI Tasks per node from 8 to 1 and maintaining the same number of two OpenMP threads per task. Results are presented in Fig. 10(a): the parallel efficiency scales efficiently up to 512 cores. As the number of cores increases, the efficiency is degraded owing to the more significant weight of MPI communications. This is mainly due to the huge memory request of the code combined with the Marconi KNL architecture. The code performance would strongly benefit from using a computer architecture with a larger RAM and a lower number of cores per node. We have also verified that the performance degradation cannot be handled by using an OpenMP strategy, as shown in Fig. 10(b), since the code performance is not

affected by increasing the number of threads per node. In summary, within the current parallelization, the best performance is achieved with 32 MPI threads and 2 OpenMP tasks per node on a KNL system.

A slightly better performance is achieved using a full $3D$ configuration with $128 \times 128 \times 64$ grid points in the spatial domain. The strong scaling from 128 to 1024 cores is shown in Fig. 10(c). A weak scaling test has been also performed by multiplying the number of spatial points and the number of cores (nodes) by the same factor. From the results, presented in Fig 10(d), it can be appreciated that the parallel efficiency is high only up to several hundreds cores.

These preliminary tests show a reasonable parallel efficiency on KNL architecture, at least up to some hundreds cores. We are presently working to increase the code efficiency, in particular optimizing the communication pattern of the ViDA algorithm. We note that these results in part depend on the employed architecture. It is worth to finally highlight that, for instance, by using a Skylake machine with 192 GB and 48 cores per node, we would be able to increase by a factor of 3 the number of spatial gridpoints per node, thus increasing the parallel efficiency of the code, as the number of communications would strongly decrease.

Concerning the computational costs, the ViDA code is about twice as computationally expensive as the HVM code (Valentini et al. 2007), which has been recently used for 3D simulations of plasma turbulence (see for instance Cerri et al. (2018)). More specifically, the reconnection run presented here – which is the most expensive test in this paper in terms of required computational resources – has a cost of slightly less than 0.1 Mh on Marconi supercomputer using 16 nodes and 512 MPI processes. On the other hand, being ViDA a code for a new piece of physics, it is difficult to foresee for the exact cost of a 3D reconnection (or turbulence) run because the numerical and physical parameters, as well as the duration of the run, can vary significantly with respect to the standard ones used with the HVM code. Based on the experience with the HVM code, we may suggest that a high resolution 3D run of magnetic reconnection focusing on the electron physics would take from a few to a few tens of Mh. Such a significant allocation of computing time can be obtained, for example, in the framework of a PRACE project.

for a new piece of physics, it is difficult to foresee for the exact cost of a 3D reconnection (or turbulence) run because the numerical and physical parameters, as well as the duration of the run, can vary significantly with respect to the standard ones used with the HVM code.

7. Conclusion

In this paper we have presented a fully-kinetic code (ViDA) based on a Vlasov-Darwin algorithm, where only light waves are excluded in order to relax the constraint on the timestep advancement. This approach is particularly suited for the investigation of the kinetic dynamics from sub-ion scales down to the electron kinetic scales d_e and to the Debye length λ_D. As typically the case for space plasmas, but often also in the laboratory, inter-particle collisions are not described, since collisional scales are assumed to be smaller than other characteristics dynamical scales.

ViDA has been tested against several waves modes, in particular Alfvén, whistlers and plasma waves. The development of the Weibel instability and reconnection, both in a regime where the main dynamics is driven by the electrons, has been also reproduced. These tests represent typical regimes of interest for studying the electron scale kinetic dynamics representing at today a strong computational challenge and a frontier problem for the understanding of the electron plasma physics.

One of the main future objectives of ViDA will be the study of the structure and dynamics of the electron diffusion region, including the role of anomalous resistivity in the Ohms law and the mechanisms of electron heating, which are among the main targets of satellite MMS data analysis (Torbert et al. 2016; Genestreti et al. 2018; Cozzani et al. 2019). Last but not least, we will make use of the ViDA code for the study of the plasma turbulent dynamics focusing on the problem of the "dissipative" scale, of primary interest in the context of the solar wind turbulent heating at kinetic scales (Vaivads et al. 2016).

This project (FC, AR, FV) has received funding from the European Unions Horizon 2020 research and innovation programme under grant agreement No 776262 (AIDA, www.aida-space.eu). OP is partly supported by the International Space Science Institute (ISSI) in the framework of the International Team 405 entitled "Current Sheets, Turbulence, Structures and Particle Acceleration in the Heliosphere". EC is partially supported by NWO Vidi grant 639.072.716. Numerical simulations discussed here have been performed on the Marconi cluster at CINECA (Italy), under the ISCRA initiative (IsC53_MRVDS and IsB16_VDMMS) and under the INAF-CINECA initiative (INA17_C2A16 and INA17_C2A16b).

REFERENCES

Barnes, A. 1966 Collisionless damping of hydromagnetic waves. *The Physics of Fluids* **9** (8), 1483–1495, arXiv: https://aip.scitation.org/doi/pdf/10.1063/1.1761882.

Birdsall, C. K. & Langdon, A. B. 2004 Plasma physics via computer simulation. CRC press.

Birn, J., Drake, J., Shay, M., Rogers, B., Denton, R., Hesse, M., Kuznetsova, M., Ma, Z., Bhattacharjee, A., Otto, A. & others 2001 Geospace environmental modeling (gem) magnetic reconnection challenge. *Journal of Geophysical Research: Space Physics* **106** (A3), 3715–3719.

Breuillard, H., Matteini, L., Argall, M. R., Sahraoui, F., Andriopoulou, M., Contel, O. L., Retinò, A., Mirioni, L., Huang, S. Y., Gershman, D. J., Ergun, R. E., Wilder, F. D., Goodrich, K. A., Ahmadi, N., Yordanova, E., Vaivads, A., Turner, D. L., Khotyaintsev, Y. V., Graham, D. B., Lindqvist, P.-A., Chasapis, A., Burch, J. L., Torbert, R. B., Russell, C. T., Magnes, W., Strangeway, R. J., Plaschke, F., Moore, T. E., Giles, B. L., Paterson, W. R., Pollock, C. J., Lavraud, B., Fuselier, S. A. & Cohen, I. J. 2018 "new insights into the nature of turbulence in the earth's magnetosheath using magnetospheric MultiScale mission data". *The Astrophysical Journal* **859** (2), 127.

Brunetti, M., Califano, F. & Pegoraro, F. 2000 Asymptotic evolution of nonlinear landau damping. *Phys. Rev. E* **62**, 4109–4114.

Bruno, R. & Carbone, V. 2016 Turbulence in the solar wind. Springer.

Burch, J. L., Moore, T. E., Torbert, R. B. & Giles, B. L. 2016 Magnetospheric Multiscale Overview and Science Objectives. *Space Sci. Rev.* **199**, 5–21.

Burch, J. L., Torbert, R. B., Phan, T. D., Chen, L.-J., Moore, T. E., Ergun, R. E., Eastwood, J. P., Gershman, D. J., Cassak, P. A., Argall, M. R., Wang, S., Hesse, M., Pollock, C. J., Giles, B. L., Nakamura, R., Mauk, B. H., Fuselier, S. A., Russell, C. T., Strangeway, R. J., Drake, J. F., Shay, M. A., Khotyaintsev, Y. V., Lindqvist, P.-A., Marklund, G., Wilder, F. D., Young, D. T., Torkar, K., Goldstein, J., Dorelli, J. C., Avanov, L. A., Oka, M., Baker, D. N., Jaynes, A. N., Goodrich, K. A., Cohen, I. J., Turner, D. L., Fennell, J. F., Blake, J. B., Clemmons, J., Goldman, M., Newman, D., Petrinec, S. M., Trattner, K. J., Lavraud, B., Reiff, P. H., Baumjohann, W., Magnes, W., Steller, M., Lewis, W., Saito, Y., Coffey, V. & Chandler, M. 2016 Electron-scale measurements of magnetic reconnection in space. *Science* **352** (6290), arXiv: http://science.sciencemag.org/content/352/6290/aaf2939.full.pdf.

Califano, F., Cerri, S., Faganello, M., Laveder, D. & Kunz, M. 2018 Electron-only magnetic reconnection in plasma turbulence. *arXiv preprint arXiv:1810.03957* .

Califano, F., Faganello, M. & Pegoraro, F. 2007 Collisionless magnetic reconnection. *Plasma Physics and Controlled Fusion* **49** (12B), B439–B446.

Califano, F., Hellinger, P., Kuznetsov, E., Passot, T., Sulem, P. L. & Trvnek, P. M. 2008 Nonlinear mirror mode dynamics: Simulations and modeling. *Journal of Geophysical Research: Space Physics* **113** (A8).

Califano, F. & Mangeney, A. 2008 A one dimensional, electrostatic vlasov model for the generation of suprathermal electron tails in solar wind conditions. *Journal of Geophysical Research: Space Physics* **113** (A6).

Camporeale, E. & Burgess, D. 2011 THE DISSIPATION OF SOLAR WIND TURBULENT FLUCTUATIONS AT ELECTRON SCALES. *The Astrophysical Journal* **730** (2), 114.

Camporeale, E. & Burgess, D. 2017 Comparison of linear modes in kinetic plasma models. *Journal of Plasma Physics* **83** (2), 535830201, arXiv: 1611.07957.

Camporeale, E. & Zimbardo, G. 2015 Wave-particle interactions with parallel whistler waves: Nonlinear and time-dependent effects revealed by particle-in-cell simulations. *Physics of Plasmas* **22** (9), 092104.

Cerri, S. S. & Califano, F. 2017 Reconnection and small-scale fields in 2D-3V hybrid-kinetic driven turbulence simulations. *New Journal of Physics* **19** (2), 025007.

Cerri, S. S., Kunz, M. W. & Califano, F. 2018 Dual phase-space cascades in 3d hybrid-vlasov–maxwell turbulence. *The Astrophysical Journal* **856** (1), L13.

Cerri, S. S., Servidio, S. & Califano, F. 2017 Kinetic cascade in solar-wind turbulence: 3d3v hybrid-kinetic simulations with electron inertia. *The Astrophysical Journal* **846** (2), L18.

Chasapis, A., Matthaeus, W. H., Parashar, T. N., Wan, M., Haggerty, C. C., Pollock, C. J., Giles, B. L., Paterson, W. R., Dorelli, J., Gershman, D. J., Torbert, R. B., Russell, C. T., Lindqvist, P.-A., Khotyaintsev, Y., Moore, T. E., Ergun, R. E. & Burch, J. L. 2018 "in situ observation of intermittent dissipation at kinetic scales in the earth's magnetosheath". *The Astrophysical Journal* **856** (1), L19.

Chen, G. & Chacón, L. 2014 An energy- and charge-conserving, nonlinearly implicit, electromagnetic 1d-3v vlasovdarwin particle-in-cell algorithm. *Computer Physics Communications* **185** (10), 2391 – 2402.

Chen, G. & Chacón, L. 2015 A multi-dimensional, energy- and charge-conserving, nonlinearly implicit, electromagnetic vlasovdarwin particle-in-cell algorithm. *Computer Physics Communications* **197**, 73 – 87.

Cheng, C.-Z. & Knorr, G. 1976 The integration of the vlasov equation in configuration space. *Journal of Computational Physics* **22** (3), 330–351.

Cozzani, G., Retinò, A., Califano, F., Alexandrova, A., Le Contel, O., Khotyaintsev, Y., Vaivads, A., Fu, H. S., Catapano, F., Breuillard, H., Ahmadi, N., Lindqvist, P.-A., Ergun, R. E., Torbert, R. B., Giles, B. L., Russell, C. T., Nakamura, R., Fuselier, S., Mauk, B. H., Moore, T. & Burch, J. L. 2019 In situ spacecraft observations of a structured electron diffusion region during magnetopause reconnection. *Phys. Rev. E* **99**, 043204.

Daughton, W., Roytershteyn, V., Karimabadi, H., Yin, L., Albright, B., Bergen, B. & Bowers, K. 2011 Role of electron physics in the development of turbulent magnetic reconnection in collisionless plasmas. *Nature Physics* **7** (7), 539–542.

Delzanno, G. 2015 Multi-dimensional, fully-implicit, spectral method for the vlasovmaxwell equations with exact conservation laws in discrete form. *Journal of Computational Physics* **301**, 338 – 356.

Divin, A., Khotyaintsev, Y. V., Vaivads, A., Andr, M., Markidis, S. & Lapenta, G. 2015 Evolution of the lower hybrid drift instability at reconnection jet front. *Journal of Geophysical Research: Space Physics* **120** (4), 2675–2690, arXiv: https://agupubs.onlinelibrary.wiley.com/doi/pdf/10.1002/2014JA020503.

Falchetto, G. L., Scott, B. D., Angelino, P., Bottino, A., Dannert, T., Grandgirard, V., Janhunen, S., Jenko, F., Jolliet, S., Kendl, A., McMillan, B. F., Naulin, V., Nielsen, A. H., Ottaviani, M., Peeters, A. G., Pueschel, M. J., Reiser, D., Ribeiro, T. T. & Romanelli, M. 2008 The european turbulence code benchmarking effort: turbulence driven by thermal gradients in magnetically confined plasmas. *Plasma Physics and Controlled Fusion* **50** (12), 124015.

Franci, L., Landi, S., Matteini, L., Verdini, A. & Hellinger, P. 2016 Plasma Beta

Dependence of the Ion-scale Spectral Break of Solar Wind Turbulence: High-resolution 2D Hybrid Simulations. *The Astrophysical Journal* **833** (1), 91, arXiv: 1610.05158.

Franci, L., Landi, S., Verdini, A., Matteini, L. & Hellinger, P. 2018 Solar wind turbulent cascade from MHD to sub-ion scales: Large-size 3d hybrid particle-in-cell simulations. *The Astrophysical Journal* **853** (1), 26.

Franci, L., Verdini, A., Matteini, L., Landi, S. & Hellinger, P. 2015 Solar Wind Turbulence from MHD to Sub-ion Scales: High-resolution Hybrid Simulations. *The Astrophys. J. Lett.* **804**, L39, arXiv: 1503.05457.

Fuselier, S. A., Lewis, W. S., Schiff, C., Ergun, R., Burch, J. L., Petrinec, S. M. & Trattner, K. J. 2016 Magnetospheric multiscale science mission profile and operations. *Space Science Reviews* **199** (1), 77–103.

Galeotti, L. & Califano, F. 2005 Asymptotic evolution of weakly collisional vlasov-poisson plasmas. *Phys. Rev. Lett.* **95**, 015002.

Galeotti, L., Califano, F. & Pegoraro, F. 2006 echography of vlasov codes. *Physics Letters A* **355** (4), 381 – 385.

Gary, S. P. & Karimabadi, H. 2006 Linear theory of electron temperature anisotropy instabilities: Whistler, mirror, and weibel. *Journal of Geophysical Research: Space Physics* **111** (A11), arXiv: https://agupubs.onlinelibrary.wiley.com/doi/pdf/10.1029/2006JA011764.

Genestreti, K. J., Varsani, A., Burch, J. L., Cassak, P. A., Torbert, R. B., Nakamura, R., Ergun, R. E., Phan, T.-D., Toledo-Redondo, S., Hesse, M., Wang, S., Giles, B. L., Russell, C. T., Vrs, Z., Hwang, K.-J., Eastwood, J. P., Lavraud, B., Escoubet, C. P., Fear, R. C., Khotyaintsev, Y., Nakamura, T. K. M., Webster, J. M. & Baumjohann, W. 2018 Mms observation of asymmetric reconnection supported by 3-d electron pressure divergence. *Journal of Geophysical Research: Space Physics* **123** (3), 1806–1821, arXiv: https://agupubs.onlinelibrary.wiley.com/doi/pdf/10.1002/2017JA025019.

Ghizzo, A., Sarrat, M. & Del Sarto, D. 2017 Vlasov models for kinetic Weibel-type instabilities. *Journal of Plasma Physics* **83** (1), 705830101.

González, C. A., Parashar, T. N., Gomez, D., Matthaeus, W. H. & Dmitruk, P. 2019 Turbulent electromagnetic fields at sub-proton scales: Two-fluid and full-kinetic plasma simulations. *Physics of Plasmas* **26** (1), 012306, arXiv: 1809.00985.

Griffiths, D. J. 1962 Introduction to electrodynamics. Prentice Hall New Jersey.

Grošelj, D., Cerri, S. S., Navarro, A. B., Willmott, C., Told, D., Loureiro, N. F., Califano, F. & Jenko, F. 2017 Fully kinetic versus reduced-kinetic modeling of collisionless plasma turbulence. *The Astrophysical Journal* **847** (1), 28.

Haggerty, C. C., Parashar, T. N., Matthaeus, W. H., Shay, M. A., Yang, Y., Wan, M., Wu, P. & Servidio, S. 2017 Exploring the statistics of magnetic reconnection x-points in kinetic particle-in-cell turbulence. *Physics of Plasmas* **24** (10), 102308, arXiv: https://doi.org/10.1063/1.5001722.

Harris, E. G. 1962 On a plasma sheath separating regions of oppositely directed magnetic field. *Il Nuovo Cimento (1955-1965)* **23** (1), 115–121.

Helander, P., Eriksson, L.-G. & Andersson, F. 2002 Runaway acceleration during magnetic reconnection in tokamaks. *Plasma Physics and Controlled Fusion* **44** (12B), B247–B262.

Hesse, M., Aunai, N., Birn, J., Cassak, P., Denton, R. E., Drake, J. F., Gombosi, T., Hoshino, M., Matthaeus, W., Sibeck, D. & Zenitani, S. 2016 Theory and modeling for the magnetospheric multiscale mission. *Space Science Reviews* **199** (1), 577–630.

Hoilijoki, S., Palmroth, M., Walsh, B. M., Pfau-Kempf, Y., vonÂ Alfthan, S., Ganse, U., Hannuksela, O. & Vainio, R. 2016 Mirror modes in the Earth's magnetosheath: Results from a global hybrid-Vlasov simulation. *Journal of Geophysical Research (Space Physics)* **121** (5), 4191–4204.

Howes, G., Dorland, W., Cowley, S., Hammett, G., Quataert, E., Schekochihin, A. & Tatsuno, T. 2008a Kinetic simulations of magnetized turbulence in astrophysical plasmas. *Physical Review Letters* **100** (6), 065004.

Howes, G. G. 2016 The Dynamical Generation of Current Sheets in Astrophysical Plasma Turbulence. *The Astrophysical Journal Letters* **827** (2), L28, arXiv: 1607.07465.

Howes, G. G., Cowley, S. C., Dorland, W., Hammett, G. W., Quataert, E. &

Schekochihin, A. A. 2008b A model of turbulence in magnetized plasmas: Implications for the dissipation range in the solar wind. *Journal of Geophysical Research: Space Physics (1978–2012)* **113** (A5).

Howes, G. G., Cowley, S. C., Dorland, W., Hammett, G. W., Quataert, E. & Schekochihin, A. e. A. 2006 Astrophysical Gyrokinetics: Basic Equations and Linear Theory. *The Astrophysical Journal* **651** (1), 590–614, arXiv: astro-ph/0511812.

Howes, G. G., Tenbarge, J. M., Dorland, W., Quataert, E., Schekochihin, A. A., Numata, R. & Tatsuno, T. 2011 Gyrokinetic Simulations of Solar Wind Turbulence from Ion to Electron Scales. *Physical Review Letters* **107** (3), 035004, arXiv: 1104.0877.

Juno, J., Hakim, A., TenBarge, J., Shi, E. & Dorland, W. 2018 Discontinuous galerkin algorithms for fully kinetic plasmas. *Journal of Computational Physics* **353**, 110 – 147.

Karimabadi, H., Roytershteyn, V., Wan, M., Matthaeus, W. H., Daughton, W., Wu, P., Shay, M., Loring, B., Borovsky, J., Leonardis, E., Chapman, S. C. & Nakamura, T. K. M. 2013 Coherent structures, intermittent turbulence, and dissipation in high-temperature plasmas. *Physics of Plasmas* **20** (1), 012303.

Kaufman, A. N. & Rostler, P. S. 1971 The Darwin Model as a Tool for Electromagnetic Plasma Simulation. *Physics of Fluids* **14** (2), 446–448.

Kempf, Y., Pokhotelov, D., von Alfthan, S., Vaivads, A., Palmroth, M. & Koskinen, H. E. J. 2013 Wave dispersion in the hybrid-Vlasov model: Verification of Vlasiator. *Physics of Plasmas* **20** (11), 112114, arXiv: 1311.3793.

Kobayashi, S., Sahraoui, F., Passot, T., Laveder, D., Sulem, P. L., Huang, S. Y., Henri, P. & Smets, R. 2017 Three-dimensional Simulations and Spacecraft Observations of Sub-ion Scale Turbulence in the Solar Wind: Influence of Landau Damping. *The Astrophysical Journal* **839** (2), 122.

Krall, N. A. & Trivelpiece, A. W. 1973 Principles of plasma physics. *American Journal of Physics* **41** (12), 1380–1381.

Kulsrud, R. M. 2005 Plasma physics for astrophysics. Princeton University Press.

Landau, L. 1946 On the vibration of the electronic plasma. *Zh. Eksp. Teor. Fiz.* **16**, 574.

Lapenta, G., Markidis, S., Goldman, M. V. & Newman, D. L. 2015 Secondary reconnection sites in reconnection-generated flux ropes and reconnection fronts. *Nature Physics* **11** (8), 690–695.

Lapenta, G., Pucci, F., Goldman, M. V. & Newman, D. L. 2019 A violin sonata for reconnection. *arXiv e-prints* p. arXiv:1904.02094, arXiv: 1904.02094.

Le Contel, O., Retinò, A., Breuillard, H., Mirioni, L., Robert, P., Chasapis, A., Lavraud, B., Chust, T., Rezeau, L., Wilder, F. D., Graham, D. B., Argall, M. R., Gershman, D. J., Lindqvist, P.-A., Khotyaintsev, Y. V., Marklund, G., Ergun, R. E., Goodrich, K. A., Burch, J. L., Torbert, R. B., Needell, J., Chutter, M., Rau, D., Dors, I., Russell, C. T., Magnes, W., Strangeway, R. J., Bromund, K. R., Leinweber, H. K., Plaschke, F., Fischer, D., Anderson, B. J., Le, G., Moore, T. E., Pollock, C. J., Giles, B. L., Dorelli, J. C., Avanov, L. & Saito, Y. 2016 Whistler mode waves and hall fields detected by mms during a dayside magnetopause crossing. *Geophysical Research Letters* **43** (12), 5943–5952, arXiv: https://agupubs.onlinelibrary.wiley.com/doi/pdf/10.1002/2016GL068968.

Leonardis, E., Chapman, S. C., Daughton, W., Roytershteyn, V. & Karimabadi, H. 2013 Identification of Intermittent Multifractal Turbulence in Fully Kinetic Simulations of Magnetic Reconnection. *Physical Review Letters* **110** (20), 205002, arXiv: 1302.1749.

Lyutikov, M. 2003 Explosive reconnection in magnetars. *Monthly Notices of the Royal Astronomical Society* **346** (2), 540–554, arXiv: http://oup.prod.sis.lan/mnras/article-pdf/346/2/540/4293592/346-2-540.pdf.

Mandt, M. E., Denton, R. E. & Drake, J. F. 1994 Transition to whistler mediated magnetic reconnection. *Geophysical Research Letters* **21** (1), 73–76, arXiv: https://agupubs.onlinelibrary.wiley.com/doi/pdf/10.1029/93GL03382.

Mangeney, A., Califano, F., Cavazzoni, C. & Travnicek, P. 2002 A numerical scheme for the integration of the vlasov–maxwell system of equations. *Journal of Computational Physics* **179** (2), 495–538.

Markidis, S., Lapenta, G. & Rizwan-uddin 2010 Multi-scale simulations of plasma with ipic3d. *Mathematics and Computers in Simulation* **80** (7), 1509 – 1519, multiscale modeling of moving interfaces in materials.

Marsch, E. 2006 Kinetic physics of the solar corona and solar wind. *Living Reviews in Solar Physics* **3** (1), 1.

Navarro, A. B. n., Teaca, B., Told, D., Groselj, D., Crandall, P. & Jenko, F. 2016 Structure of plasma heating in gyrokinetic alfvénic turbulence. *Phys. Rev. Lett.* **117**, 245101.

O'Neil, T. 1965 Collisionless damping of nonlinear plasma oscillations. *The Physics of Fluids* **8** (12), 2255–2262, arXiv: https://aip.scitation.org/doi/pdf/10.1063/1.1761193.

Palmroth, M., Ganse, U., Pfau-Kempf, Y., Battarbee, M., Turc, L., Brito, T., Grand in, M., Hoilijoki, S., Sandroos, A. & von Alfthan, S. 2018 Vlasov methods in space physics and astrophysics. *Living Reviews in Computational Astrophysics* **4** (1), 1, arXiv: 1808.05885.

Palmroth, M., Honkonen, I., Sandroos, A., Kempf, Y., von Alfthan, S. & Pokhotelov, D. 2013 Preliminary testing of global hybrid-Vlasov simulation: Magnetosheath and cusps under northward interplanetary magnetic field. *Journal of Atmospheric and Solar-Terrestrial Physics* **99**, 41–46.

Palodhi, L., Califano, F. & Pegoraro, F. 2009 Nonlinear kinetic development of the weibel instability and the generation of electrostatic coherent structures. *Plasma Physics and Controlled Fusion* **51** (12), 125006.

Palodhi, L., Califano, F. & Pegoraro, F. 2010 On the transition between the weibel and the whistler instabilities. *Plasma Physics and Controlled Fusion* **52** (9), 095007.

Parashar, T. N., Matthaeus, W. H. & Shay, M. A. 2018 Dependence of Kinetic Plasma Turbulence on Plasma β. *The Astrophysical Journal* **864** (1), L21, arXiv: 1807.11371.

Parashar, T. N., Shay, M. A., Cassak, P. A. & Matthaeus, W. H. 2009 Kinetic dissipation and anisotropic heating in a turbulent collisionless plasma. *Physics of Plasmas* **16** (3), 032310, arXiv: https://doi.org/10.1063/1.3094062.

Passot, T. & Sulem, P. L. 2007 Collisionless magnetohydrodynamics with gyrokinetic effects. *Physics of Plasmas* **14** (8), 082502.

Perrone, D., Passot, T., Laveder, D., Valentini, F., Sulem, P. L., Zouganelis, I., Veltri, P. & Servidio, S. 2018 Fluid simulations of plasma turbulence at ion scales: Comparison with vlasov-maxwell simulations. *Physics of Plasmas* **25** (5), 052302, arXiv: https://doi.org/10.1063/1.5026656.

Peyret, R. & Taylor, T. D. 1986 Computational methods for fluid flow. Springer Series in Computational Physics (Springer, New York, 1983).

Pezzi, O., Parashar, T. N., Servidio, S., Valentini, F., Vásconez, C. L., Yang, Y., Malara, F., Matthaeus, W. H. & Veltri, P. 2017a Colliding alfvénic wave packets in magnetohydrodynamics, hall and kineticsimulations. *Journal of Plasma Physics* **83** (1), 705830108.

Pezzi, O., Parashar, T. N., Servidio, S., Valentini, F., Vásconez, C. L., Yang, Y., Malara, F., Matthaeus, W. H. & Veltri, P. 2017b Revisiting a classic: The parkermoffatt problem. *The Astrophysical Journal* **834** (2), 166.

Pezzi, O., Perrone, D., Servidio, S., Valentini, F., Sorriso-Valvo, L. & Veltri, P. 2019 Proton-proton collisions in the turbulent solar wind: Hybrid Boltzmann-Maxwell simulations. *arXiv e-prints* p. arXiv:1903.03398, arXiv: 1903.03398.

Pezzi, O., Servidio, S., Perrone, D., Valentini, F., Sorriso-Valvo, L., Greco, A., Matthaeus, W. H. & Veltri, P. 2018 Velocity-space cascade in magnetized plasmas: Numerical simulations. *Physics of Plasmas* **25** (6), 060704, arXiv: https://doi.org/10.1063/1.5027685.

Pezzi, O., Valentini, F. & Veltri, P. 2016 Collisional Relaxation of Fine Velocity Structures in Plasmas. *Physical Review Letters* **116** (14), 145001.

Pfau-Kempf, Y., Battarbee, M., Ganse, U., Hoilijoki, S., Turc, L., von Alfthan, S., Vainio, R. & Palmroth, M. 2018 On the importance of spatial and velocity resolution in the hybrid-Vlasov modeling of collisionless shocks. *Frontiers in Physics* **6**, 44.

Phan, T., Eastwood, J. P., Shay, M., Drake, J., Sonnerup, B. Ö., Fujimoto, M., Cassak, P., Øieroset, M., Burch, J., Torbert, R. & others 2018 Electron magnetic reconnection without ion coupling in earths turbulent magnetosheath. *Nature* **557** (7704), 202.

Pokhotelov, D., von Alfthan, S., Kempf, Y., Vainio, R., Koskinen, H. E. J. &

Palmroth, M. 2013 Ion distributions upstream and downstream of the Earth's bow shock: first results from Vlasiator. *Annales Geophysicae* **31** (12), 2207–2212.

Pritchett, P. 2008 Collisionless magnetic reconnection in an asymmetric current sheet. *Journal of Geophysical Research: Space Physics* **113** (A6).

Pritchett, P. L. 2001 Geospace Environment Modeling magnetic reconnection challenge: Simulations with a full particle electromagnetic code. *J. Geophys. Res.* **106**, 3783–3798.

Pucci, F., Matthaeus, W. H., Chasapis, A., Servidio, S., Sorriso-Valvo, L., Olshevsky, V., Newman, D. L., Goldman, M. V. & Lapenta, G. 2018 Generation of turbulence in colliding reconnection jets. *The Astrophysical Journal* **867** (1), 10.

Pucci, F., Servidio, S., Sorriso-Valvo, L., Olshevsky, V., Matthaeus, W. H., Malara, F., Goldman, M. V., Newman, D. L. & Lapenta, G. 2017 Properties of turbulence in the reconnection exhaust: Numerical simulations compared with observations. *The Astrophysical Journal* **841** (1), 60.

Retinò, A., Sundkvist, D., Vaivads, A., Mozer, F., André, M. & Owen, C. J. 2007 In situ evidence of magnetic reconnection in turbulent plasma. *Nature Physics* **3**, 236–238.

Rincon, F., Califano, F., Schekochihin, A. A. & Valentini, F. 2016 Turbulent dynamo in a collisionless plasma. *Proceedings of the National Academy of Sciences* **113** (15), 3950–3953, arXiv: https://www.pnas.org/content/113/15/3950.full.pdf.

Roytershteyn, V., Boldyrev, S., Delzanno, G. L., Chen, C. H. K., Grošelj, D. & Loureiro, N. F. 2019 Numerical Study of Inertial Kinetic-Alfvén Turbulence. *The Astrophysical Journal* **870** (2), 103.

Schekochihin, A. A., Cowley, S. C., Dorland, W., Hammett, G. W., Howes, G. G., Plunk, G. G., Quataert, E. & Tatsuno, T. 2008 Gyrokinetic turbulence: a nonlinear route to dissipation through phase space. *Plasma Physics and Controlled Fusion* **50** (12), 124024, arXiv: 0806.1069.

Schmitz, H. & Grauer, R. 2006a Darwin–vlasov simulations of magnetised plasmas. *Journal of Computational Physics* **214** (2), 738–756.

Schmitz, H. & Grauer, R. 2006b Kinetic vlasov simulations of collisionless magnetic reconnection. *Physics of plasmas* **13** (9), 092309.

Servidio, S., Chasapis, A., Matthaeus, W. H., Perrone, D., Valentini, F., Parashar, T. N., Veltri, P., Gershman, D., Russell, C. T., Giles, B., Fuselier, S. A., Phan, T. D. & Burch, J. 2017 Magnetospheric multiscale observation of plasma velocity-space cascade: Hermite representation and theory. *Phys. Rev. Lett.* **119**, 205101.

Servidio, S., Matthaeus, W. H., Shay, M. A., Cassak, P. A. & Dmitruk, P. 2009 Magnetic Reconnection in Two-Dimensional Magnetohydrodynamic Turbulence. *Physical Review Letters* **102** (11), 115003.

Servidio, S., Matthaeus, W. H., Shay, M. A., Dmitruk, P., Cassak, P. A. & Wan, M. 2010 Statistics of magnetic reconnection in two-dimensional magnetohydrodynamic turbulence. *Physics of Plasmas* **17** (3), 032315, arXiv: https://doi.org/10.1063/1.3368798.

Servidio, S., Valentini, F., Califano, F. & Veltri, P. 2012 Local Kinetic Effects in Two-Dimensional Plasma Turbulence. *Physical Review Letters* **108** (4), 045001.

Servidio, S., Valentini, F., Perrone, D., Greco, A., Califano, F., Matthaeus, W. H. & Veltri, P. 2015 A kinetic model of plasma turbulence. *Journal of Plasma Physics* **81** (1), 325810107.

Shay, M. A., Drake, J. F., Rogers, B. N. & Denton, R. E. 2001 Alfvnic collisionless magnetic reconnection and the hall term. *Journal of Geophysical Research: Space Physics* **106** (A3), 3759–3772, arXiv: https://agupubs.onlinelibrary.wiley.com/doi/pdf/10.1029/1999JA001007.

Shay, M. A., Haggerty, C. C., Matthaeus, W. H., Parashar, T. N., Wan, M. & Wu, P. 2018 Turbulent heating due to magnetic reconnection. *Physics of Plasmas* **25** (1), 012304.

Skoutnev, V., Hakim, A., Juno, J. & TenBarge, J. M. 2019 Temperature-dependent Saturation of Weibel-type Instabilities in Counter-streaming Plasmas. *The Astrophysical Journal Letters* **872** (2), L28, arXiv: 1902.08672.

Sorriso-Valvo, L., Carbone, F., Perri, S., Greco, A., Marino, R. & Bruno, R. 2018a On the statistical properties of turbulent energy transfer rate in the inner heliosphere. *Solar Physics* **293** (1), 10.

Sorriso-Valvo, L., Catapano, F., Retinò, A., Le Contel, O., Perrone, D., Roberts,

O. W., Coburn, J. T., Panebianco, V., Valentini, F., Perri, S., Greco, A., Malara, F., Carbone, V., Veltri, P., Pezzi, O., Fraternale, F., Di Mare, F., Marino, R., Giles, B., Moore, T. E., Russell, C. T., Torbert, R. B., Burch, J. L. & Khotyaintsev, Y. V. 2019 Turbulence-driven ion beams in the magnetospheric kelvin-helmholtz instability. *Phys. Rev. Lett.* **122**, 035102.

Sorriso-Valvo, L., Perrone, D., Pezzi, O., Valentini, F., Servidio, S., Zouganelis, I. & Veltri, P. 2018b Local energy transfer rate and kinetic processes: the fate of turbulent energy in two-dimensional hybrid vlasovmaxwell numerical simulations. *Journal of Plasma Physics* **84** (2), 725840201.

Sulem, P. L. & Passot, T. 2015 Landau fluid closures with nonlinear large-scale finite Larmor radius corrections for collisionless plasmas. *Journal of Plasma Physics* **81** (1), 325810103.

Sulem, P. L., Passot, T., Laveder, D. & Borgogno, D. 2016 Influence of the Nonlinearity Parameter on the Solar Wind Sub-ion Magnetic Energy Spectrum: FLR-Landau Fluid Simulations. *The Astrophysical Journal* **818** (1), 66, arXiv: 1511.01256.

Tanabe, H., Yamada, T., Watanabe, T., Gi, K., Kadowaki, K., Inomoto, M., Imazawa, R., Gryaznevich, M., Michael, C., Crowley, B., Conway, N. J., Scannell, R., Harrison, J., Fitzgerald, I., Meakins, A., Hawkes, N., McClements, K. G., O'Gorman, T., Cheng, C. Z. & Ono, Y. 2015 Electron and ion heating characteristics during magnetic reconnection in the mast spherical tokamak. *Phys. Rev. Lett.* **115**, 215004.

Tatsuno, T., Dorland, W., Schekochihin, A. A., Plunk, G. G., Barnes, M., Cowley, S. C. & Howes, G. G. 2009 Nonlinear Phase Mixing and Phase-Space Cascade of Entropy in Gyrokinetic Plasma Turbulence. *Physical Review Letters* **103** (1), 015003, arXiv: 0811.2538.

TenBarge, J. M., Howes, G. G. & Dorland, W. 2013 Collisionless Damping at Electron Scales in Solar Wind Turbulence. *The Astrophysical Journal* **774** (2), 139.

Told, D., Jenko, F., TenBarge, J. M., Howes, G. G. & Hammett, G. W. 2015 Multiscale Nature of the Dissipation Range in Gyrokinetic Simulations of Alfvénic Turbulence. *Physical Review Letters* **115** (2), 025003, arXiv: 1505.02204.

Torbert, R. B., Burch, J. L., Giles, B. L., Gershman, D., Pollock, C. J., Dorelli, J., Avanov, L., Argall, M. R., Shuster, J., Strangeway, R. J., Russell, C. T., Ergun, R. E., Wilder, F. D., Goodrich, K., Faith, H. A., Farrugia, C. J., Lindqvist, P.-A., Phan, T., Khotyaintsev, Y., Moore, T. E., Marklund, G., Daughton, W., Magnes, W., Kletzing, C. A. & Bounds, S. 2016 Estimates of terms in ohm's law during an encounter with an electron diffusion region. *Geophysical Research Letters* **43** (12), 5918–5925, arXiv: https://agupubs.onlinelibrary.wiley.com/doi/pdf/10.1002/2016GL069553.

Torbert, R. B., Burch, J. L., Phan, T. D., Hesse, M., Argall, M. R., Shuster, J., Ergun, R. E., Alm, L., Nakamura, R., Genestreti, K. J., Gershman, D. J., Paterson, W. R., Turner, D. L., Cohen, I., Giles, B. L., Pollock, C. J., Wang, S., Chen, L.-J., Stawarz, J. E., Eastwood, J. P., Hwang, K. J., Farrugia, C., Dors, I., Vaith, H., Mouikis, C., Ardakani, A., Mauk, B. H., Fuselier, S. A., Russell, C. T., Strangeway, R. J., Moore, T. E., Drake, J. F., Shay, M. A., Khotyaintsev, Y. V., Lindqvist, P.-A., Baumjohann, W., Wilder, F. D., Ahmadi, N., Dorelli, J. C., Avanov, L. A., Oka, M., Baker, D. N., Fennell, J. F., Blake, J. B., Jaynes, A. N., Le Contel, O., Petrinec, S. M., Lavraud, B. & Saito, Y. 2018 Electron-scale dynamics of the diffusion region during symmetric magnetic reconnection in space. *Science* **362** (6421), 1391–1395, arXiv: https://science.sciencemag.org/content/362/6421/1391.full.pdf.

Tronci, C. & Camporeale, E. 2015 Neutral vlasov kinetic theory of magnetized plasmas. *Physics of Plasmas* **22** (2), 020704, arXiv: https://doi.org/10.1063/1.4907665.

Umeda, T., Miwa, J.-i., Matsumoto, Y., Nakamura, T. K. M., Togano, K., Fukazawa, K. & Shinohara, I. 2010 Full electromagnetic Vlasov code simulation of the Kelvin-Helmholtz instability. *Physics of Plasmas* **17** (5), 052311.

Umeda, T., Togano, K. & Ogino, T. 2009 Two-dimensional full-electromagnetic Vlasov code with conservative scheme and its application to magnetic reconnection. *Computer Physics Communications* **180** (3), 365–374.

Umeda, T. & Wada, Y. 2016 Secondary instabilities in the collisionless Rayleigh-Taylor instability: Full kinetic simulation. *Physics of Plasmas* **23** (11), 112117.

Umeda, T. & Wada, Y. 2017 Non-MHD effects in the nonlinear development of the MHD-scale Rayleigh-Taylor instability. *Physics of Plasmas* **24** (7), 072307.

Uzdensky, D. A. 2011 Magnetic reconnection in extreme astrophysical environments. *Space Science Reviews* **160** (1), 45–71.

Uzdensky, D. A. & Kulsrud, R. M. 2006 Physical origin of the quadrupole out-of-plane magnetic field in hall-magnetohydrodynamic reconnection. *Physics of Plasmas* **13** (6), 062305, arXiv: https://doi.org/10.1063/1.2209627.

Vaivads, A., Retinò, A., Soucek, J., Khotyaintsev, Y. V., Valentini, F., Escoubet, C. P., Alexandrova, O., André, M., Bale, S. D., Balikhin, M. & et al. 2016 Turbulence heating observer satellite mission proposal. *Journal of Plasma Physics* **82** (5), 905820501.

Valentini, F., Califano, F. & Veltri, P. 2010 Two-dimensional kinetic turbulence in the solar wind. *Phys. Rev. Lett.* **104**, 205002.

Valentini, F., Carbone, V., Veltri, P. & Mangeney, A. 2005 Self-consistent Lagrangian study of nonlinear Landau damping. *Phys. Rev. E* **71** (1), 017402.

Valentini, F., Perrone, D., Stabile, S., Pezzi, O., Servidio, S., Marco, R. D., Marcucci, F., Bruno, R., Lavraud, B., Keyser, J. D., Consolini, G., Brienza, D., Sorriso-Valvo, L., Retinò, A., Vaivads, A., Salatti, M. & Veltri, P. 2016 Differential kinetic dynamics and heating of ions in the turbulent solar wind. *New Journal of Physics* **18** (12), 125001.

Valentini, F., Trávníček, P., Califano, F., Hellinger, P. & Mangeney, A. 2007 A hybrid-vlasov model based on the current advance method for the simulation of collisionless magnetized plasma. *Journal of Computational Physics* **225** (1), 753–770.

Valentini, F., Vásconez, C. L., Pezzi, O., Servidio, S., Malara, F. & Pucci, F. 2017 Transition to kinetic turbulence at proton scales driven by large-amplitude kinetic alfvén fluctuations. *"Astronomy and Astrophysics"* **599**, "A8".

Vàsconez, C. L., Valentini, F., Camporeale, E. & Veltri, P. 2014 Vlasov simulations of kinetic alfvn waves at proton kinetic scales. *Physics of Plasmas* **21** (11), 112107, arXiv: https://doi.org/10.1063/1.490158.

Von Alfthan, S., Pokhotelov, D., Kempf, Y., Hoilijoki, S., Honkonen, I., Sandroos, A. & Palmroth, M. 2014 Vlasiator: First global hybrid-vlasov simulations of earth's foreshock and magnetosheath. *Journal of Atmospheric and Solar-Terrestrial Physics* **120**, 24–35.

Wan, M., Matthaeus, W. H., Roytershteyn, V., Karimabadi, H., Parashar, T., Wu, P. & Shay, M. 2015 Intermittent Dissipation and Heating in 3D Kinetic Plasma Turbulence. *Physical Review Letters* **114** (17), 175002.

Weibel, E. S. 1959 Spontaneously Growing Transverse Waves in a Plasma Due to an Anisotropic Velocity Distribution. *Physical Review Letters* **2**, 83–84.

Yang, Y., Matthaeus, W. H., Parashar, T. N., Haggerty, C. C., Roytershteyn, V., Daughton, W., Wan, M., Shi, Y. & Chen, S. 2017 Energy transfer, pressure tensor, and heating of kinetic plasma. *Physics of Plasmas* **24** (7), 072306, arXiv: https://doi.org/10.1063/1.4990421.

Zeiler, A., Biskamp, D., Drake, J. F., Rogers, B. N., Shay, M. A. & Scholer, M. 2002 Three-dimensional particle simulations of collisionless magnetic reconnection. *Journal of Geophysical Research: Space Physics* **107** (A9), SMP 6–1–SMP 6–9, arXiv: https://agupubs.onlinelibrary.wiley.com/doi/pdf/10.1029/2001JA000287.